

# A Free-Form Lensing Grid Solution for A1689 with New Multiple Images

Jose M. Diego<sup>1\*</sup>, T. Broadhurst<sup>2,3</sup>, N. Benitez<sup>4</sup>, K. Umetsu<sup>5</sup>, D. Coe<sup>6</sup>, I. Sendra<sup>2</sup>, M. Sereno<sup>7</sup>, L. Izzo<sup>8</sup>, G. Covone<sup>9,10</sup>

<sup>1</sup>*IFCA, Instituto de Física de Cantabria (UC-CSIC), Av. de Los Castros s/n, 39005 Santander, Spain*

<sup>2</sup>*Fisika Teorikoa, Zientzia eta Teknologia Fakultatea, Euskal Herriko Unibertsitatea UPV/EHU*

<sup>3</sup>*IKERBASQUE, Basque Foundation for Science, Alameda Urquijo, 36-5 48008 Bilbao Spain*

<sup>4</sup>*Instituto de Astrofísica de Andalucía (CSIC), Apdo. 3044, 18008 Granada, Spain*

<sup>5</sup>*Institute of Astronomy and Astrophysics, Academia Sinica, P.O. Box 23-141, Taipei 10617, Taiwan*

<sup>6</sup>*Space Telescope Science Institute, Baltimore, MD, USA*

<sup>7</sup>*Dipartimento di Fisica e Astronomia, Università di Bologna, Viale Berti Pichat 6/2, 40127 Bologna, Italia*

<sup>8</sup>*Dipartimento di Fisica, Sapienza Università di Roma and ICRA, p.le A. Moro 2, I-00185 Rome, Italy*

<sup>9</sup>*Dipartimento di Fisica, Università di Napoli Federico II, Via Cinthia, I-80126 Napoli, Italy*

<sup>10</sup>*INFN Sez. di Napoli, Compl. Univ. Monte S. Angelo, Via Cinthia, I-80126 Napoli, Italy*

Draft version 1 November 2021

## ABSTRACT

Hubble Space Telescope imaging of the galaxy cluster Abell 1689 has revealed an exceptional number of strongly lensed multiply-imaged galaxies, including high-redshift candidates. Previous studies have used this data to obtain the most detailed dark matter reconstructions of any galaxy cluster to date, resolving substructures 25 kpc across. We examine Abell 1689 (hereafter, A1689) non-parametrically, combining strongly lensed images and weak distortions from wider field Subaru imaging, and we incorporate member galaxies to improve the lens solution. Strongly lensed galaxies are often locally affected by member galaxies, however, these perturbations cannot be recovered in grid based reconstructions because the lensing information is too sparse to resolve member galaxies. By adding luminosity-scaled member galaxy deflections to our smooth grid we can derive meaningful solutions with sufficient accuracy to permit the identification of our own strongly lensed images, so our model becomes self consistent. We identify 11 new multiply lensed system candidates and clarify previously ambiguous cases, in the deepest optical and NIR data to date from Hubble and Subaru. Our improved spatial resolution brings up new features not seen when the weak and strong lensing effects are used separately, including clumps and filamentary dark matter around the main halo. Our treatment means we can obtain an objective mass ratio between the cluster and galaxy components, for examining the extent of tidal stripping of the luminous member galaxies. We find a typical mass-to-light ratios of  $M/L_B = 21 \pm 14$  inside the  $r < 1$  arcminute region that drops to  $M/L_B = 17 \pm 8$  inside the  $r < 40$  arcsecond region. Our model independence means we can objectively evaluate the competitiveness of stacking cluster lenses for defining the geometric lensing-distance-redshift relation in a model independent way.

**Key words:** galaxies:clusters:general; galaxies:clusters:A1689; methods:data analysis; dark matter

## 1 INTRODUCTION

A fuller exploration of non-parametric cluster lensing is increasingly motivated by new dedicated deep Hubble imaging surveys, with the aim of examining dark matter structures in the least biased way. Multiple sets of lensed images are now typically identified in deep, high resolution images of any cosmologically distant cluster imaged with Hubble, allowing

systematic exploration of the cluster dark matter and discovery of the most distant galaxies (Broadhurst & et al. 2005a; Clowe et al. 2006; Coe et al. 2010, 2012, 2013; Zitrin et al. 2009, 2010, 2011; Zheng et al. 2012). In practice, secure identification of multiple images need the guidance of a reasonably accurate lens model as even the counter images of large arcs are typically hard to find given the complexities

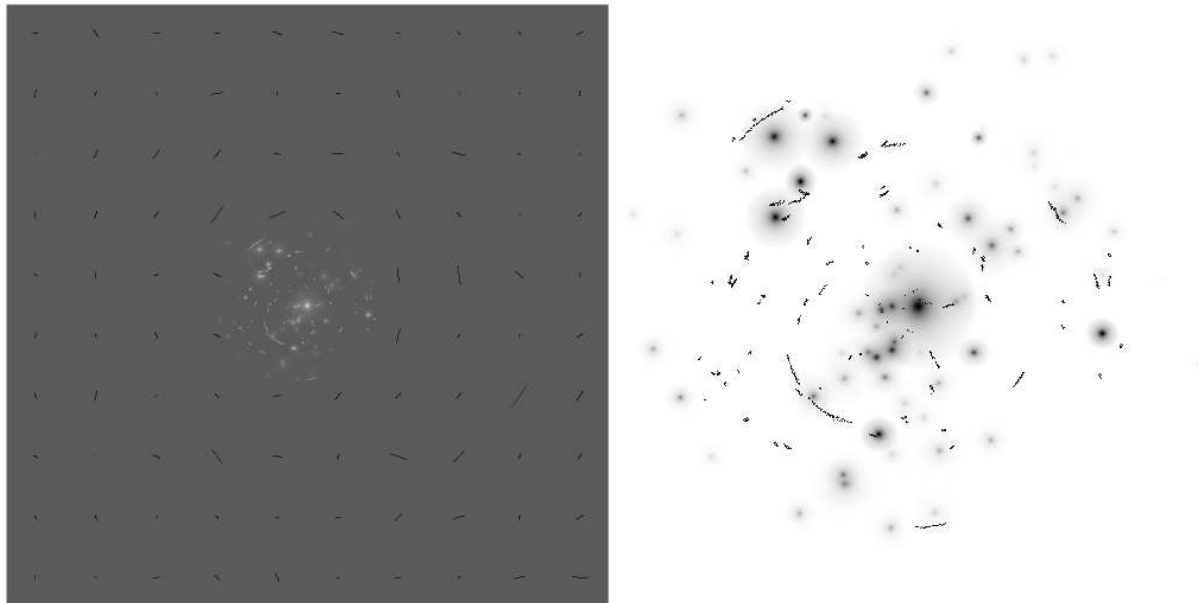


**Figure 1.** Data set used for the reconstruction. The left panel shows the entire field of view of  $10'$  where the strong lensing arcs are represented in white and the reduced shear measurements are represented in black. The position of the galaxies and their shapes are represented in light grey. The right panel shows the central  $3.33'$  region with the arcs and galaxies in non-linear scale to better show the extent of the galaxy haloes in our model.

in the central mass distribution of clusters, so that images for a given source are far from symmetrically located.

Furthermore, the uncertain redshifts of faint lensed images means that even when a reliable mass model can be built, counter images are predicted to fall on long, largely radial loci or may fail to be generated at all if the unknown source distance is insufficient. This means that there are often several contending counter images unless internal colors and morphology are sufficiently distinctive. Photometric redshifts, if unambiguous, are very helpful in limiting the selection of counter images that are too faint for spectroscopy. The 16 overlapping broad bands of the CLASH program covering the UV to the NIR, maximises the photometric redshift accuracy possible with Hubble and have provided reliable examples of the most distant galaxies known, as in the case of the  $z \simeq 11$  candidate lensed by MACS0647 (Coe et al. 2013), where multiple images are identified both photometrically and geometrically.

To date, the galaxy cluster A1689 remains the best studied cosmic lens with hundreds of magnified images in the central region visible in deep Hubble images (Broadhurst & et al. 2005a). Over a hundred of these arcs have been matched to their corresponding background galaxies by several authors and their redshifts estimated (Broadhurst & et al. 2005a; Halkola, Seitz & Pannella 2006; Limousin et al. 2007; Coe et al. 2010), including several of the brightest highest redshift galaxies known, extending to  $z \simeq 7.6$  (Frye, Broadhurst & Benítez 2002; Bradley et al. 2008). The relaxed appearance of this cluster and the relatively undisturbed optical and X-ray morphology has made this a preferred target for constraining the equilibrium mass profile by several independent means (Lemze et al. 2008; Sereno et al. 2013).

Several studies have used these arcs to reconstruct the mass distribution using the strong lens-

ing data alone (Broadhurst & et al. 2005a; Diego et al. 2005b; Halkola, Seitz & Pannella 2006; Jullo & Kneib 2009; Coe et al. 2010) and in combination with weak lensing (or WL hereafter) measurements (Broadhurst et al. 2005b; Limousin et al. 2007; Umetsu & Broadhurst 2008) including the use of background red galaxies whose surface density is depleted by lens magnification and independent observationally from weak lensing shear. A1689 has been studied also using higher order derivatives of the lensing potential, like the flexion (see (Leonard, King & Goldberg 2011) for a recent analysis) The mass profile of A1689 was shown to be very well fitted by the standard NFW profile describing the equilibrium mass distribution expected for collisionless, cold dark matter (CDM) (Broadhurst & et al. 2005a; Broadhurst et al. 2005b) but with a concentration that is surprisingly high. Triaxiality of the mass distribution has been explored as a means of boosting projected concentrations, and certainly may be expected to be partially responsible (Oguri et al. 2005; Broadhurst & Barkana 2008; Sereno et al. 2013).

A1689 has been subsequently followed at other wavelengths, allowing lensing to be combined with SZ and X-ray data (Sereno et al. 2013) and also with the dynamics of member galaxy motions via the Jeans equation and via velocity caustics (Lemze et al. 2009). Multiwavelength science opens the door to new exciting studies since it is no longer sufficient to model the mass or gas separately but instead both have to be integrated in the same model in order to explain the observations. Previous work on A1689 combines HST and *Chandra* and reveals some tension between hydrostatic+lensing reconstruction and other observations (Zekser et al. 2006; Leonard et al. 2007; Umetsu & Broadhurst 2008; Cain, Schechter & Bautz 2011; Sereno & Umetsu 2011; Lemze et al. 2008). Peng et al. (2009) finds a discrepant hydrostatic mass based on X-ray

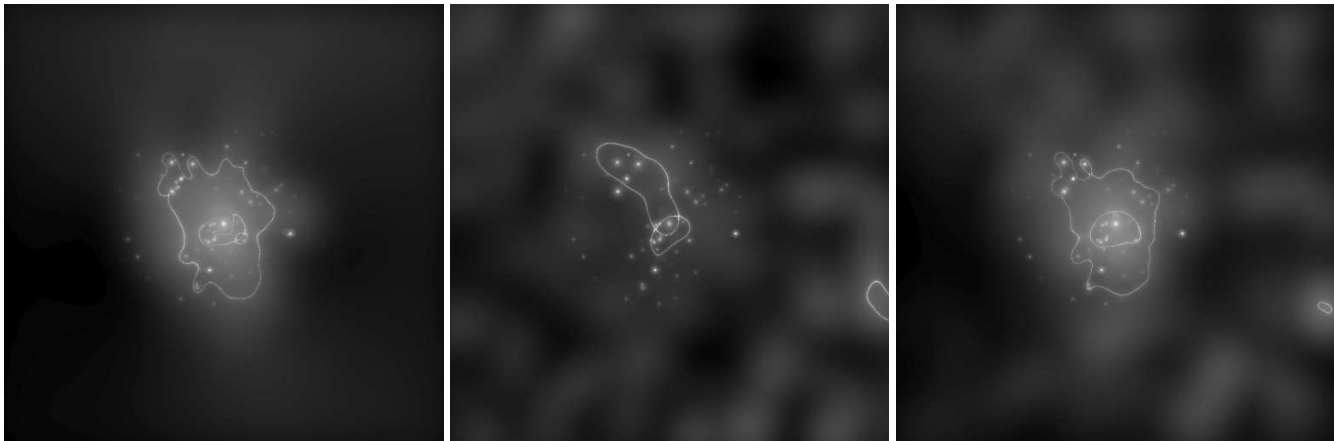


**Figure 2.** Solutions (and associated critical curves for a source at redshift  $z=2$ ) for the cases where only the SL data is used in the reconstruction (left), only the WL data is used in the reconstruction (center) and both, the SL and WL data are used in the reconstruction (right). In all cases only the central  $6.66 \times 6.66$  arcmin<sup>2</sup> region is shown.

data from *Chandra* but Riemer-Sørensen et al. (2009) find that excluding substructure alleviates or even eliminates the discrepancy. Lensing data combined with X-ray and SZ data have the potential to reveal information not only about the *invisible* dark matter distribution but also about the physical phenomena taking place in the cluster that have to bring the gas pressure and dark-matter-driven gravity to a quasi-equilibrium state. The new Frontier Fields program<sup>1</sup> is now underway to provide the deepest Hubble data ever recorded for massive lensing clusters, further motivating our assumption-free modeling.

Despite exhausting lensing studies of A1689, many arcs still remain unmatched for this cluster. Certainly, many missing counterimages of highly magnified images are too faint to be useful or remain undetected. Others are of too low contrast to be detected within the light of luminous cluster members. Inaccuracy of mass models used to reconstruct the mass distribution is another issue, given the significant variation between published solutions. In Ponente & Diego (2011), the authors show how very erroneous mass distributions can still reproduce lensing data to high accuracy. In other words, being able to reproduce the observed arcs is no guarantee that the reconstructed mass distribution is right. The most detailed analysis made using A1689 strong lensing data, and that have been able to match tens of arcs, have relied either on the distribution of member galaxies to guide the models or on parametric models with the inclusion of many parameters depending on the number of substructures adopted.

However, the persistent resistance of some obvious bright lensed images to be matched with other images (when the same models predict another bright counterpart for those lensed images) suggests that these models are still missing fundamental pieces that allows to solve the puzzle. One of the limitations of strong lensing data is that it quickly becomes insensitive to the mass distribution beyond the Einstein radius, especially if the distribution of matter around the center is more or less spherical. Clumps with a significant amount of matter that lie just beyond the

Einstein radius might go unnoticed with these parametric models as the model contains enough parameters within the Einstein radius to easily fit the data. Attempts have been made to constrain the matter distribution beyond the Einstein radius of A1689 by combining the weak lensing data with strong lensing data but in all cases (to the best of our knowledge) these *joint* analysis have been made a posteriori where either the density profiles are combined to extract a single density profile (Umetsu & Broadhurst 2008) or the SL solution is tested against the WL data for consistency (Limousin et al. 2007).

In this paper we revisit this cluster to obtain a truly joint solution combining in a single inversion (i.e. not *a posteriori*) the SL and WL data. By doing this, our 2-dimensional model of the mass distribution has to account simultaneously for the multiple lensed systems observed in A1689 and for the shear measurements that extend well beyond the Einstein radius.

## 2 ACS DATA

In this paper we used public imaging data obtained from the ACS (filters: F450W and F814W) and the WFC3 (filter F125W), retrieved from the Mikulski Archive for Space Telescope (MAST). The data come from two different programs. The F814W (ACS) and F125W (WFC3) data were obtained within the HST program 11718 (PI Blakeslee, Cycle 17), from May 29 to July 8 of 2010, while the ACS F475W images were obtained within the program 9289 (PI Fors, Cycle 11) on June 16 2002. The total exposure time is 9500 s, 75172 s and 14367 s in the F450W, F814W and F125W filters, respectively. The F814W dataset has been independently reduced and used by Alamo-Martínez et al. (2013) to study the intracluster population of globular clusters. The data reduction of the optical data consisted in two main steps, based mostly on *multidrizzle* (Koekemoer & et al. 2002)<sup>2</sup>.

<sup>2</sup> *multidrizzle* is a software tool developed by the Science Software Branch at the STSCI and it is appositely designed for to the combination of dithered images and rejection of cosmic rays.

<sup>1</sup> <http://www.stsci.edu/hst/campaigns/frontier-fields/>

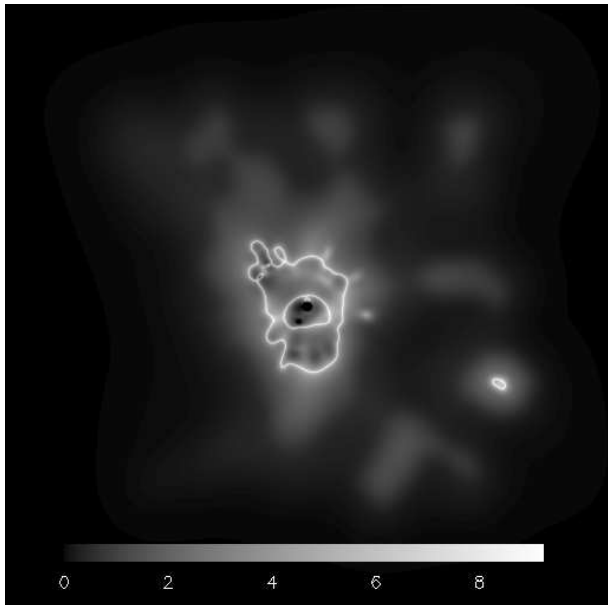


**Figure 3.** Magnification map in the entire field of view of  $10 \times 10$  arcmin<sup>2</sup> for the SL+WL case. The colors are in log-scale to increase contrast. The two small black regions in the centre correspond to magnifications less than 1 (that have been set to 0 in the log-scale for contrast purposes). The drop in the outer region (buffer zone) is a systematic effect due to the larger cell size in the grid. The features close to the phase transition region between the two grid resolutions are not always to be trusted.

First, we combined the images obtained in each run and optimized the image sampling. Then, we performed cosmic-rays rejection and aligned images<sup>3</sup>. Final mosaic has pixel scale 0.05 arcsec. We combined these three bands images to produce the color image of the new candidate lenses shown in the Appendix.

### 3 LENSING DATA ON A1689

A compilation of systems found in the literature is shown in table 2 in the appendix. They are obtained basically from 3 sources, Broadhurst & et al. (2005a), Limousin et al. (2007) and Coe et al. (2010). Many of these systems are also listed in Halkola, Seitz & Pannella (2006). Table 2 is built after cross-correlating the original tables in the references above to avoid repetitions. Systems that were listed originally in Broadhurst & et al. (2005a) are referred as B05 in table 2. Systems that appear in both Limousin et al. (2007) and Coe et al. (2010) or just in Coe et al. (2010) are listed as C10. Systems that appear only in Limousin et al. (2007) are listed as L07 and the new system candidates presented in this paper are listed as D14 in table 2. Some of the original systems in Broadhurst & et al. (2005a) were rearranged or updated with additional arclets by other authors in later papers after comparison with alternative mass models. In the present paper we will rely on the original selection of Broadhurst & et al. (2005a) after excluding some dubious systems but will explore also the solutions obtained after

incorporating the alternative systems published in the literature. The exclusion (or re-arrangement) of some systems listed in table 2 is made after a new visual color and morphology comparison of the system members based on the new and deep ACS images. For instance, the confusion between systems 10 and 12 can be resolved by the presence of a pinkish core in system 10 not present in system 12. Different authors ((Limousin et al. 2007) and (Coe et al. 2010)) have suggested alternative rearrangements for some of these systems. Although we do not consider all the alternative possibilities in this paper, they might be perfectly valid as well. In fact, as will be shown later, some of the new counterimages discovered by other authors (like in system 12) will be naturally predicted/confirmed by our model, and hence, fully consistent with it. If the system was listed in Broadhurst & et al. (2005a) we maintain the system identification from Broadhurst & et al. (2005a). Alternative identifications of the central counterimages of some systems have been used in Limousin et al. (2007) and Coe et al. (2010). Some of these alternative identifications are also reflected in table 2. Although not explicitly mentioned in the table 2, the last system in Halkola, Seitz & Pannella (2006) corresponds (at least partially) to our system 58 in table 2. The last 11 systems of table 2 (denoted with D14 in the REF column of table 2) should be treated just as mere candidates since they are obtained after identifying new system candidates using our solution discussed below and without a proper photometric redshift estimation. The new candidate systems are shown in figures A1 and A2 in the appendix. The stamps are extracted from a RGB composite image of 3 Hubble filters (F475w, F814w and the near infrared F125w). Some of the positions listed in Coe et al. (2010) were also incorrectly translated into the tex file in the original paper. These positions have been corrected in table 2. Table 2 contains a total of 50 systems.<sup>4</sup> Systems 25 and 32 contain multiple candidates for some of the secondary images and will not be used in our analysis. Out of the 50 systems listed in table 2, we use only a reliable subset of 26 systems corresponding to systems 1 through 30 in Broadhurst & et al. (2005a) but excluding suspicious systems 20, 26, 27 (in addition to system 25 mentioned above) System 10 and 12 have been re-matched after examination of new IR data that exhibit distinctive colors.

Our WL data are derived from Umetsu & Broadhurst (2008) based on Subaru  $V_i'$  imaging observations, and we refer the reader to that paper for a detailed description of their observations and analysis. In this work, we use two-dimensional reduced-shear data on a regular grid of  $10 \times 10$  independent grid points with  $1'$  spacing, covering the central  $10 \times 10$  arcmin<sup>2</sup> region. We exclude from our analysis the innermost four pixels overlapping with the critical-lensing regime, so that our WL data set consists of  $100 - 4 = 96$  reduced-shear data points. Since the fields of view and orientations of the HST and Subaru data sets are different (in their native form), we rotate and re-centre the SL data to match the centroid and orientation of the WL data. Figure 1 (left) shows the two data sets used in this paper as well as the distribution (and morphology) of member galaxies that

<sup>3</sup> This step was performed by using the IRAF-geomap package

<sup>4</sup> A full set of stamps from this table can be found at <http://max.ifca.unican.es/diego/FigsA1689/>

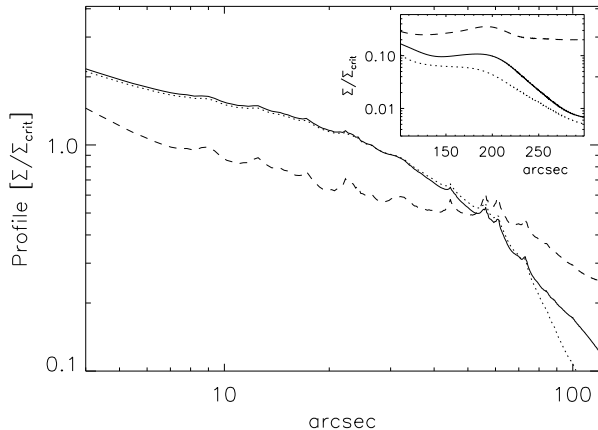


**Figure 4.** Profiles of the solutions obtained with SL data only (dotted), WL data only (dashed) and the combination SL+WL (solid). The smaller plot shows the same profiles but in linear scale and beyond  $100''$ . The units in the axis are the same as the larger plot. The systematic bump at  $200''$  (or  $3.33'$ ) coincides with the position of the transition phase (for the grid) between the  $6.66'$  region and the outer buffer zone

will be used to build the fiducial deflection field (see the next section). The right panel shows the central  $3.3 \times 3.3$  arcmin<sup>2</sup> region (WL data not shown).

#### 4 RECONSTRUCTION METHOD

We use the improved method, WSLAP+, to combine the weak and strong lensing data and perform the mass reconstruction. The reader can find the details of the method in our previous papers (Diego et al. 2005a,b, 2007; Ponente & Diego 2011; Sendra et al. 2014). Here we give a brief summary of the most essential elements.

Given the standard lens equation,

$$\beta = \theta - \alpha(\theta, \Sigma(\theta)), \quad (1)$$

where  $\theta$  is the observed position of the source,  $\alpha$  is the deflection angle,  $\Sigma(\theta)$  is the surface mass density of the cluster at the position  $\theta$ , and  $\beta$  is the position of the background source. Both the strong lensing and weak lensing observables can be expressed in terms of derivatives of the lensing potential.

$$\psi(\theta) = \frac{4GD_l D_{ls}}{c^2 D_s} \int d^2\theta' \Sigma(\theta') \ln(|\theta - \theta'|), \quad (2)$$

where  $D_l$ ,  $D_{ls}$  and  $D_s$  are the angular diameter distances to the lens, from the lens to the source and from the observer to the source, respectively. The unknowns of the lensing problem are in general the surface mass density and the positions of the background sources. As shown in Diego et al. (2007), the weak and strong lensing problem can be expressed as a system of linear equations that can be represented in a compact form,

$$\Theta = \Gamma X, \quad (3)$$

where the measured strong and weak lensing observables are

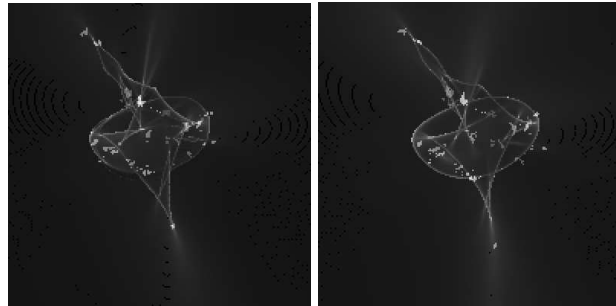


**Figure 5.** Caustics for the SL only (left) and SL+WL case (right) compared with the reconstructed sources. Each source is represented with a different color index from 1 (darkest grey) to 26 (lightest grey). The field of view corresponds to  $1.3'$  across. The centre is the same in both cases and corresponds to the centre of the original  $10'$  field of view.

contained in the array  $\Theta$  of dimension  $N_\Theta = 2N_{SL} + 2N_{WL}$ , the unknown surface mass density and source positions are in the array  $X$  of dimension  $N_X = N_c + N_g + 2N_s$  and the matrix  $\Gamma$  is known (for a given grid configuration and fiducial galaxy deflection field, see below) and has dimension  $N_\Theta \times N_X$ .  $N_{SL}$  is the number of strong lensing observables (each one contributing with two constraints,  $x$ , and  $y$ )  $N_{WL}$  is the number of weak lensing observables (each one contributing with two constraints,  $\gamma_1$ , and  $\gamma_2$ ),  $N_c$  is the number of grid points (or cells) that we use to divide the field of view.  $N_g$  is the number of deflection fields (from cluster members) that we consider.  $N_s$  is the number of background sources (each contributes with two unknowns,  $\beta_x$ , and  $\beta_y$ , see Sendra et al. (2014) for details). The solution is found after minimizing a quadratic function that estimates the solution of the system of equations 3. For this minimization we use a quadratic algorithm which is optimized for solutions with the constraint that the solution,  $X$ , must be positive. This is particularly important since by imposing this constraint we avoid the unphysical situation where the masses associated to the galaxies are negative (that could otherwise provide a reasonable solution, from the formal mathematical point of view, to the system of linear equations 3). Imposing the constrain  $X > 0$  also helps in regularizing the solution as it avoids large negative and positive contiguous fluctuations.

Earlier work has shown how the addition of the small deflection fields from member galaxies can help improve the mass determination when enough constraints are available (see for instance Kassiola, Kovner & Fort (1992), Kneib et al. (1996)). In our previous paper (Sendra et al. 2014) we quantified via simulations how the addition of deflections from all the main member galaxies helps improve the mass reconstruction with respect to our previous standard non-parametric method. For our study we select the 73 brightest elliptical galaxies (from the red sequence) in the cluster central region and associate to them a mass according to their luminosity. We assume the fiducial deflection field comprising these member galaxies just scales by a fixed luminosity–mass ratio. Later, the fitting procedure determines this proportionality constant that allows for the best reproduction of the data. In Sendra et al. (2014) we used one deflection field to model all the galaxies in the cluster. In the case of A1689 we go a step further and we use two deflection fields (i.e  $N_g = 2$ , see definition of  $N_g$

above). The first one is associated to the central type-cD galaxy and the second one contains the deflection field from the remaining dominant galaxies in the cluster. Each deflection field contributes in our model as one free parameter (its amplitude with respect to the fiducial amplitude). In principle one could incorporate an independent deflection field for each one of the member galaxies but caution has to be taken to maintain as much as possible the orthogonality between the grid cells and the individual deflection fields. However, this is an interesting alternative that will be explored further in the future. Settling for two deflection fields may be regarded as a fair compromise between the overly simple assumption that all galaxies in the cluster have individual halos with masses that trace light following the same luminosity-mass relation and a potentially more realistic but also unnecessarily complex assumption that each galaxy has a different luminosity-mass ratio. We make an exception for the central cD galaxy because of its distinctive shallow luminosity profile and the separate origin that may be implied by the anomalously large numbers of globular clusters for this object and cD galaxies in general (see Alamo-Martínez et al. (2013)). All the galaxies used in our fiducial model are shown in figure 1 where we use a non-linear color scale to better show the extent and shapes of the individual halos in our fiducial model. As in our previous paper (Sendra et al. 2014), we consider truncated NFW profiles to construct our fiducial model.

## 5 RESULTS

When combining the WL and SL data sets, due to the large field of view ( $10 \times 10$  arcminutes<sup>2</sup> sampled with a total of  $1536^2$  pixels), and in order to maximize the resolution of the grid in the region covering the SL part of the data, we use a two resolution grid where the central  $6.66 \times 6.66$  arcmin<sup>2</sup> is sampled with cells of  $24 \times 24$  pixels and the remaining area is sampled with  $64 \times 64$  pixels cells. The use of a multiresolution grid introduces a bias in the reconstruction (see discussion below) in the transition region between the two resolutions. The outer region is used as a buffer zone that, however, still contributes to the WL constraints in the transition phase between the two regions. Hence, we don't use the results from the outer region in our conclusions but instead we will restrict ourselves to the central  $6.66 \times 6.66$  arcmin<sup>2</sup> region. However, we should note that even within the central region caution has to be taken when interpreting the results close to the transition phase as some biases are still present near the border.

For comparison purposes, we have performed the reconstruction in three different cases depending on the data set used. In case (i) we use only the SL data set, in case (ii) we use only the WL data set, and in case (iii) we combine the SL and WL data set into the same data vector. In order to make a direct comparison, we use the same grid for all three cases although this is not optimal for the SL nor WL case. In the SL-only case, we would use only a regular grid covering a smaller field of view (of  $3 \times 3$  arcmin<sup>2</sup>) while in the case of the WL-only case we would also use a regular grid (with poorer resolution) but over the entire  $10 \times 10$  arcmin<sup>2</sup> field of view. Since our main interest is on the solution obtained when the SL and WL data sets are combined, we

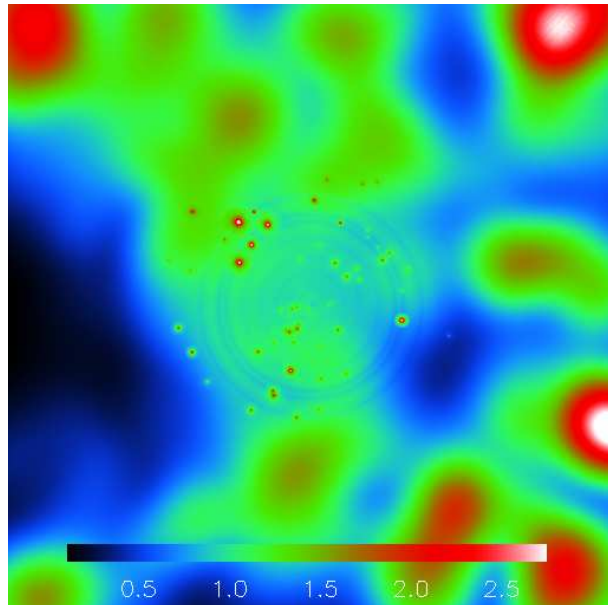


**Figure 6.** Asymmetric behaviour of the mass density in the central region of  $6.66 \times 6.66$  arcmin<sup>2</sup>. The plot shows the ratio between the solution 2D map (SL+WL case) and the corresponding profile, that is, each pixel at a distance  $r$  from the centre is divided by the profile at the same  $r$ . In order to increase contrast the ratio is saturated beyond the value 7.5 and we show the square root of this ratio.

maintain the same grid configuration in all three cases. Also, we start the minimization in the same initial condition to eliminate this degree of freedom from the solution (different initial conditions are explored later in the paper). Finally, we use the same number of iterations (8000 iterations, this number will be discussed later) in the SL-only and SL+WL cases. For the WL-only case we stop the minimization before to avoid over-fitting (a large number of iterations in the WL-only case would produce a solution that is capable of reproducing the noisy WL estimates so the minimization must be stopped before this regime is reached). In figure 2 we present the 2D reconstructed mass in the central region and the associated critical curves for a source at redshift 2 for the three cases. From left to right we show the cases of the SL-only, WL-only and SL+WL. Note how the critical curve does not change much in the case SL+WL when compared with the SL-only case. This is a consequence of the critical curve being much more sensitive to the very central region (and the SL data). However, when the WL data is used in combination with the SL data, new interesting features in the mass distribution emerge even beyond the Einstein radius. Some of these features appear even more intriguing when looking at the magnification map (see figure 3) where some filamentary structures and clumps are made more evident. Both the projected mass and magnification maps are closely connected and the magnification map in this weaker lensing regime can be used as an alternative tracer of the mass especially in the range of interest shown in figure 3 where the convergence,  $\kappa < 0.5$ , and  $\kappa \sim \gamma$ . In this regime, and to first order, the magnification,  $\mu$ , can be approximated (by Taylor expansion) as  $\mu \approx 1 + 2\kappa$  that shows the clear connection between magnification and

projected mass. Further investigation of these features demands better quality WL data and will be the subject of future studies. The small critical curve around the clump at the edge of the bottom right quadrant is close to a feature seen also in Umetsu & Broadhurst (2008). This fact suggests that the feature in our reconstruction, although it could be affected by its proximity to the buffer zone, may also be produced by an enhancement in the magnitude of the WL signal in that area.

A more quantitative comparison of the different solutions is shown in figure 4 where we show the density profiles of the surface mass density in terms of critical density. Unless otherwise noted, the critical density,  $\Sigma_{crit} = 4.746 \times 10^{15} M_{\odot} h / Mpc^2$ , is computed for  $z_{mean} = 1.07$  (as in previous work). The WL-only case shows the typical mass-sheet degeneracy which has not been corrected in our solution. Also, in the WL-only solution, the mass at the centre is mostly associated with the individual galaxies accounting for the shear in the vicinity of the Einstein radius, while the grid complements the central galaxy mass. On the other hand, in the SL-only case, the grid plays a more central role and accounts for most of the mass. Also, the SL-only case shows a sharp drop in mass beyond the Einstein radius, which is expected for this grid based model, due to the lack of sensitivity of the SL data to the outer regions. When the SL and WL data sets are combined in the joint reconstruction, the new joint profile shows a smoother behaviour to larger radius and the solution compares well with previous estimates of the profile derived from SL-only and WL-only. Both grid and galaxies play important roles in fitting the SL+WL data set.

In terms of source reconstruction, figure 5 shows the reconstructed sources for the two cases, SL-only (left) and SL+WL (right). Both, scale and image's centre are the same. In both cases, the solutions obtained with SL-only and SL+WL data seem to be able to form  $1'' - 3''$  sources that fall near well defined caustics.

In figure 6 we show the ratio between the 2D reconstructed mass map and the corresponding profile. A circularly symmetric mass distribution should behave as a constant sheet of value  $Ratio = 1$ . Deviations from this value highlight the asymmetries in different regions of the cluster. Note how the central region exhibits a more symmetric structure but around the Einstein radius there are important deviations from the mean profile by a factor  $\approx 4$  above and below the mean density. The largest deviations occur near the buffer zone, and may be affected by the proximity to this transition phase. Overall, a left-right global asymmetry (or gradient) is appreciated across the field of view. A similar asymmetry can also be found in Umetsu & Broadhurst (2008). The rings around the centre are due to the individual galaxies which produce spikes in the profile.

### 5.1 Comparison with previous results and analytical models

It is important to compare the results obtained with our non-parametric algorithm with those obtained using fully parametric methods but a similar data set. Figure 7 shows our solution compared with two analytical models that fit solutions obtained by parametric methods. Broadhurst et al. (2005b) found that in detail the NFW profile did not fit

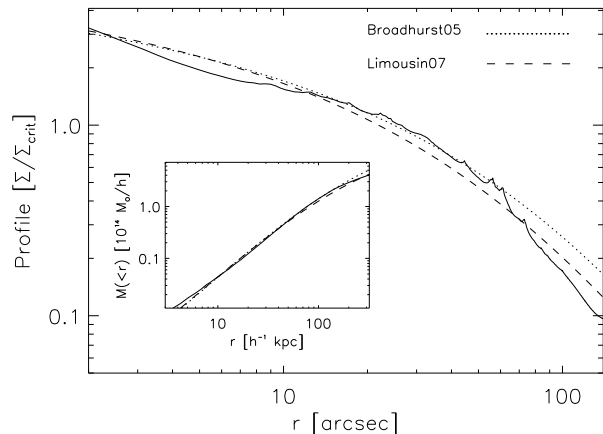


**Figure 7.** Comparison of the profile corresponding to the SL+WL solution (after 8000 iterations) with two NFW models found in the literature, and that fit their corresponding solutions (Broadhurst et al. 2005b; Limousin et al. 2007)

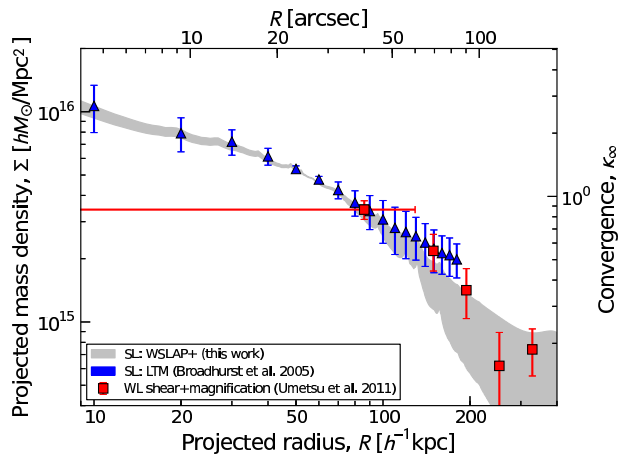


**Figure 8.** Comparison of the profiles from our solution (grey region from table 1) with previous results from the literature.

well the SL+WL data in a fashion similar to our case, with a tendency to be too steep in the center ( $r < 50$  kpc).

In figure 8 we compare the radial mass profile derived from our solution with previously published results of A1689 based on different lensing techniques. In the SL regime, our solution overlaps well with the SL modeling results of Broadhurst et al. (2005a). Our results are also in good agreement with the model-independent mass profile of Umetsu et al. (2011) derived from combined WL shear-and-magnification measurements based on the Subaru data. When compared with previous work, we find a good agreement between our solution and other solutions, in terms of the profile and the location and shape of the radial critical curve. Although the tangential critical curve we obtain extends further to the south than previous SL solutions.

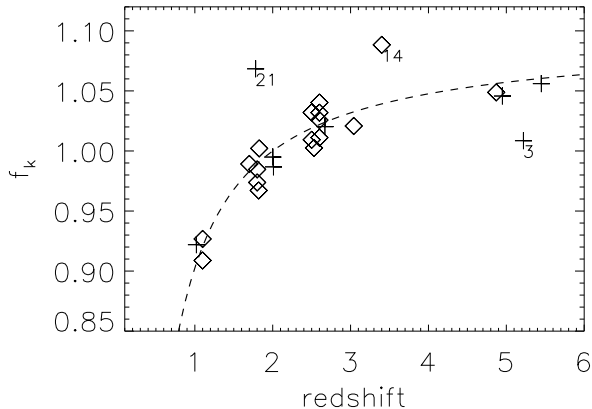


**Figure 9.** The dashed line corresponds to the function  $f_k$  for a flat model ( $\Omega_m = 0.3$ ,  $\Lambda = 0.7$ ) compared with the data (diamonds correspond to systems with spectroscopic redshifts and crosses to systems with photometric redshifts). The main outliers are marked with their corresponding ID.

## 5.2 Mass-to-light ratios

Since our mass model has the galaxy member component differentiated from the diffuse dark matter halo component we can compute light-to-mass ratios at the position of the member galaxies. We compute the luminosity (B-Johnson) of the galaxies over the same area covered by our fiducial mass model. The mass-to-light ratio oscillates around a typical value of around 20 for most of the galaxies, with a small decrease towards the central galaxy. In particular, we find a mass-to-light ratio of  $M/L_B = 21 \pm 14$  inside the  $r < 1$  arcminute region that drops to  $M/L_B = 17 \pm 8$  inside the  $r < 40$  arcsecond region. Recently, Okabe et al. (2013) found that at large cluster radii, the mass-to-light ratio of sub-halos in the Coma cluster tend to the typical values for clusters (around 200), whereas this ratio decreases towards the centre of the cluster to values around  $M/L_B \approx 35$  (for  $h = 0.7$ ) (see also, (Natarajan et al. 2009)). The fact that our critical curves present a smoother form when compared to previous estimations (see for instance Broadhurst & et al. (2005a); Halkola, Seitz & Pannella (2006); Limousin et al. (2007); Coe et al. (2010)) while the total mass inside the Einstein radius is consistent with previous work, suggesting that the masses associated to the individual galaxies in our solution are smaller than the corresponding masses derived from alternative methods. The mass-to-light ratio inferred from our solution is therefore probably smaller than the one that could be derived from those alternative methods.

## 6 COSMOLOGICAL IMPLICATIONS

Gravitational lensing in well studied clusters like A1689 can be used to impose constraints in the cosmological model (see for instance (Jullo et al. 2010)). A test based on the relative differences of the deflection angle between pairs of images was applied to A1689 in Broadhurst & et al. (2005a) based on the solution obtained with a parametric model. Figure 9 shows the  $f_k = D_{ls}(z)D_z(z_s = 2)/D_s(z)D_{ls}(z_s = 2)$  func-

tion as described in Broadhurst & et al. (2005a) (see eqs. 7 and 14 in that paper). This function is normalized for convenience to  $z = 2$  and the shape is determined by the cosmological model. Each data point correspond to a multiply lensed system (out of our set of 26). Due to the more unprecise reconstruction in the very centre of the cluster, we exclude images that are at a distance of 5 arcseconds or less from the centre. Triangles correspond to the spectroscopic redshift systems and cross symbols to those with only photometric redshifts. The dashed line indicates the expected behaviour of our data points for a standard cosmological model (flat  $\Lambda$ CDM model with  $\Omega_m = 0.3$ ). In the ideal scenario where there is no projection effects and we are able to reconstruct the deflection field perfectly, the data points would lie perfectly along the curve for the correct choice of cosmological model. Some scatter is seen here about this expected relation. The symmetry of the scatter indicates that the deflection field we recover is not noise free and imperfections and projection effects along the line of sight unrelated to the cluster must at some level limit the accuracy of this comparison. However, it is important to notice that our result is obtained with just one cluster and is not optimized for in terms of the "best" multiply lensed systems. For instance, 3 systems are marked in the above plot that depart more significantly from the expected theoretical behaviour. System number 3 corresponds to a system with only a photometric redshift (and this redshift could be wrong) and besides, two of the images of this system are relatively close to each other (this close proximity of course enhances the uncertainty in estimating  $f_k$  for such systems) and the third image is basically buried behind one of the large elliptical galaxies (and hence very sensitive to the exact mass distribution of this member galaxy at a level not incorporated in our member galaxy model. A similar situation is found in system 21, where two radial images are close to the centre (although farther than the 5 arcsecond exclusion radius mentioned above) and one of them is very close to one of the member elliptical galaxies. System 14 corresponds to a system that lies well beyond the Einstein radius, where our reconstruction is less well constrained. It is obvious from the above plot that a more accurate description of the lens (for instance through the addition of new spectroscopic systems, especially at high redshift) would permit a tighter constraint on the cosmological model. A study based on stacking  $f_k$  for many lensing clusters should be able to provide competitive constraints on the cosmological model based on this potentially important independent test, for which some simulations have been explored (Lubini et al. 2014).

## 7 VARIABILITY OF THE POSSIBLE SOLUTIONS

We refer to the best fit model presented above as our *reference solution* since in the context of this form of modeling there is no single unique solution, given that the number of lensed images and the grid resolution are finite. So more important than finding a statistically *best* solution is to understand the range of possible solutions that are consistent with the data. Hence, as discussed in previous papers, (Diego et al. 2005a,b, 2007; Ponente & Diego 2011; Sendra et al. 2014), we intentionally seek an approximate



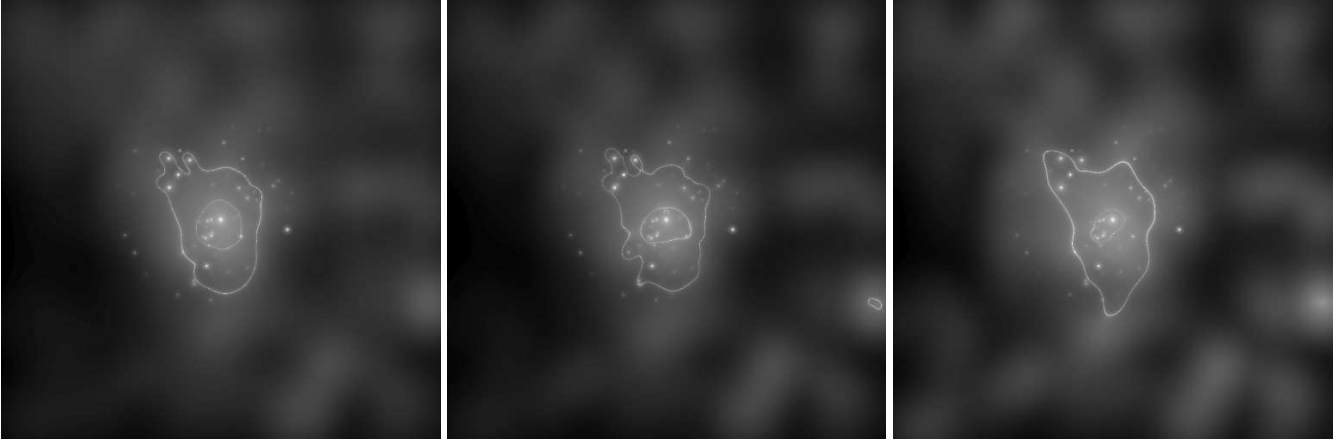


**Figure 10.** Solutions (and associated critical curves for a source at redshift  $z=2$ ) for three different iteration numbers. Left corresponds to 5000 iterations, middle to 8000 iterations and right to 15000 iterations. Note how for 8000 iterations both radial and tangential critical curves fall very close to radial and tangential arcs.

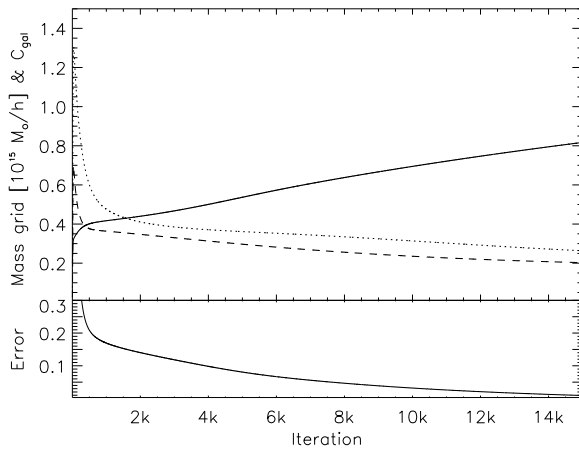


**Figure 11.** Top panel. Total mass in the grid (solid line) versus iteration number (from 1 to 15000). The dotted and dashed lines show the two coefficients  $C_1$  and  $C_2$  respectively. These coefficients multiply the fiducial fields for the type-cD ( $C_2$ ) galaxy and the remaining galaxies ( $C_1$ ). The bottom panel shows the value of the function that is being minimized as a function of iteration number (the units have been re-scaled by a constant for clarity purposes)

solution to the system of equations. A major mistake in this form of modeling is to adopt a grid of higher resolution than justified by the number of lensed images, as then in the limit we may obtain what appear to be a near perfect solution that matches identically the locations of all lensed images but at the expense of a mass distribution that is much more highly structured on small scales that is physically reasonable, including negative surface densities. Such forced solutions tend to predict sources (in the source plane) that are unreasonably small and concentrated together in the centre of the field of view corresponding to huge lens magnifications. This over-fitting regime can be avoided by appreciating that uncertainties in the data and the approximations made by our non-parametric reconstruction means that a minimal, inevitable level error must be allowed in the

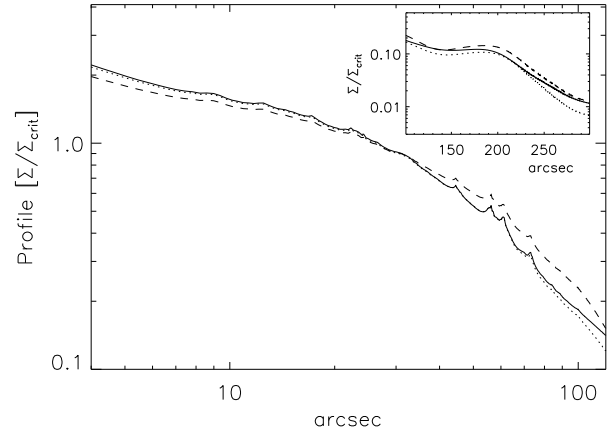


**Figure 12.** Convergence profiles for the 3 cases shown in figure 10. The solid line corresponds to the 5000 iteration case, the dotted line to the 8000 iteration case, and dashed line to the 15000 iteration case. Again, the smaller sub-plot shows the tails of these distributions across the transition phase and up to the 5' maximum radius.

reconstruction. This includes our assumptions and approximations introduced from our hypothesis that the member galaxy deflections are strictly proportional to the light, and that the soft component can be exactly modeled by a superposition of Gaussians of a given pixel scale, or that the sources in the source plane are delta functions, or that there are no significant projection of matter along the line of sight etc.

To allow for some error we may terminate the minimization at a given point as described below and beyond which further iteration may result in unreasonably structured mass distributions. Since we are minimizing a  $N_x$ -dimensional quadratic function (where the number of dimensions is the number of variables in the vector  $X$ ), after a fixed number of iterations (the number of iterations can be defined a priori) the algorithm stops in one of the infinite points contained in the  $N_x$ -dimensional circumference at a height  $\epsilon$  from the

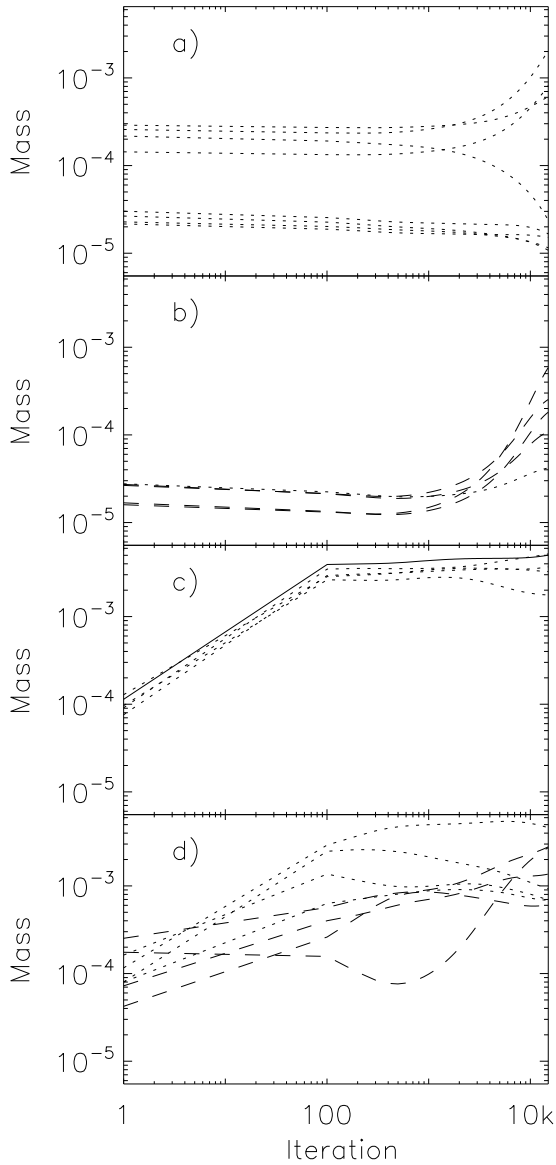


**Figure 13.** Evolution of the mass value (in units of  $10^{15} M_{\odot}/h$  per cell) in specific cells with the iteration number. From top to bottom, panel a) shows the mass in the outer edge of the buffer zone. The curves correspond to 4 contiguous  $64 \times 64$  pixel cells located at the bottom left corner of the  $10 \times 10$  arcmin<sup>2</sup> field of view (bottom set of 4 curves) and 4 contiguous  $64 \times 64$  pixel cells in the opposite corner at the top-right corner of the field of view (top set of 4 curves). Panel b) shows as a dotted line the case of a  $64 \times 64$  pixel cell situated in the interior edge of the buffer zone. In particular this cell is at the diagonal and at the transition phase between resolutions. The dashed lines correspond to the 4 closest  $24 \times 24$  pixel cells to the  $64 \times 64$  pixel cell. Panel c) shows with a solid line the cell situated in the centre of the field of view. The four dotted lines are the 4 cells immediately to the right-left and up-down from the central cell. Panel d) shows the case of 4 cells situated at  $0.5'$  from the centre (dotted lines) and at  $1'$  from the centre (dashed lines).

minimum of the quadratic function. The value of  $\epsilon$  can be estimated (and hence the maximum number of iterations) if we set a prior on the mean size of the galaxies in the source plane and we combine this information with the error in the shear measurements (see Diego et al. (2005a)). We also generate simulated data-sets that mimic the data so that we can determine an optimal range for the number of iterations that best reconstructs the input model, as described in Sendra et al. (2014). The starting point for the iteration process is also important as different initial conditions may imply the most reasonable point to stop iterating.

As our input catalog we consider first a reliable set of 26 robust strongly lensed systems in which we have great faith. Some of these systems have only photometric redshifts which can be imprecise. Changing the SL (or WL) data set has an impact on the reconstructed solution as the constraints in the system change accordingly. In this section we explore these sources of variability. Other sources of variability still exist including the number of grid cells to adopt or changing the parameters that define the deflection field of the member galaxies.

### 7.1 Dependency with iteration number

The maximum number of iterations chosen determines some of the properties of the solution. In Sendra et al. (2014) we discussed how for a simulated data set of SL measurements that was designed to resemble the real data of A1689, the optimal number of iterations was of the order of several thousands. Also, an interesting conclusion from that work is that by incorporating the deflection field of the galaxies, one gets the added bonus of increasing the stability of the solution which tends to saturate to a fixed minimum level of precision as the number of iterations becomes very large. The over-fitting problem was reduced as well but nevertheless, over-fitting can occur if the number of iterations is too large so the algorithm always needs to be stopped after a given number of iterations. For this purpose, we have found that using the location of the radial critical curves is a sensitive choice for identifying a sensible range for the number of iterations, as the radius of this critical curve is well defined in the data as it can be seen to be fairly circular in shape from the distribution of very radially extended images. This is not the case for the tangential critical curve.

In this paper, this part of the analysis is done a posteriori (although it could be in principle incorporated into the system of linear equations, however, this is beyond the scope of this work and will be studied in more detail in a future paper). In figure 10 we show three solutions corresponding to three different numbers of iterations (where the number of parameters fitted and the initial condition in the minimization are identical between these three solutions). From left to right we show the solutions obtained after 5000, 8000 and 15000 iterations. By looking at the tangential curves, the three cases look different but they still accommodate well the large tangential arcs in between the tangential critical curve. The radial curve, on the other hand, when compared with the position of key well identified radial arcs, is clearly too large in the case of 5000 iterations and too small in the case of 15000 iterations. In contrast, the case of 8000 iterations, the radial critical curve (computed for  $z=2$ ) overlaps almost perfectly with the mean position of differ-

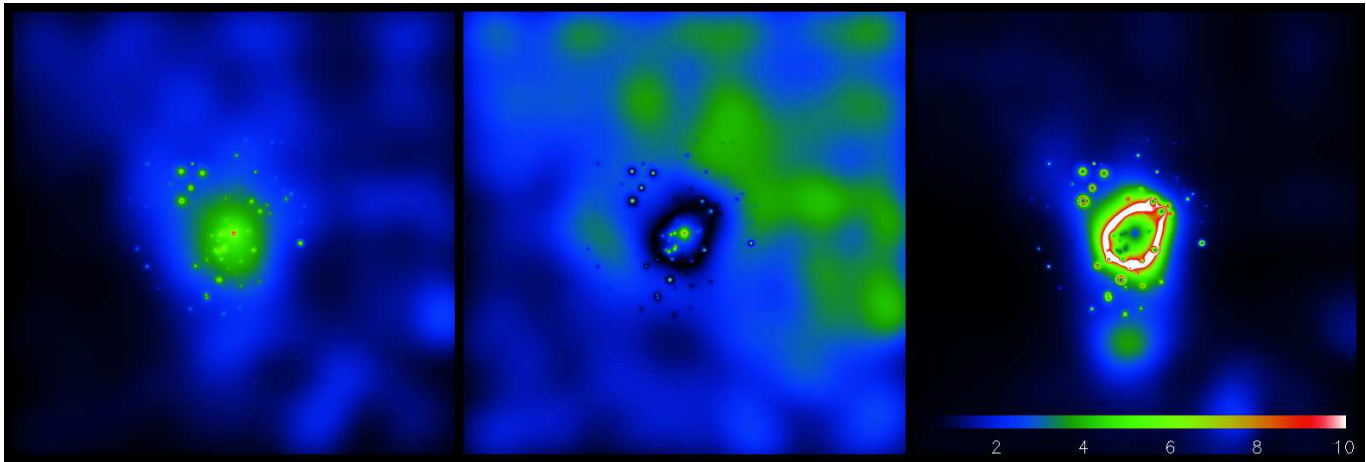


**Figure 14.** Reconstructed average mass from 40 independent solutions in the 10 arcminute field of view (left panel). The middle panel shows the dispersion of these solutions. The right panel shows the SNR map defined as the average map (left panel) divided by the dispersion map (middle panel). The SNR vary between SNR=0.7 at its minimum and SNR=290 at its maximum (but saturated in this plot above SNR=100). All maps are shown as the square root (in order to increase contrast) and the color scale (shown in the right panel) is the same in all panels.

ent radial arcs present in the cluster at redshifts  $z \approx 2$ . This simple comparison seems to indicate that the best solutions are obtained with our code after  $\sim 8000$  iterations. Using the radial critical curve as a way of determining the optimal range of iterations can be also seen as a regularization of our problem. This is an interesting alternative since it is solely based on actual data.

An idea of the dependency of the solution with the number of iterations can be obtained also from figure 11. In the top part of this plot we represent the total mass contained in the grid (solid line) versus the iteration number. The solid and dashed lines represent the correction factors  $C_1$  and  $C_2$ , that are applied to the fiducial deflection fields from the galaxies. As the iteration number grows, there starts to be a trade between the mass contained in the grid, and the mass in the galaxies but the total mass (especially in the central region) stays more or less constant beyond a few thousand iterations as can be seen better from the profiles (figure 12). A similar trend was observed when applying the method to simulated data (Sendra et al. 2014). As the iteration number grows, the solution increases its complexity in order to concentrate the arcs into smaller sources. As the fiducial field has only two degrees of freedom ( $C_1$  and  $C_2$ ), new features appear only in the grid part of the solution at the expense of reducing the mass in the member galaxies to keep the total mass more or less constant (within the Einstein radius). Of course, and as mentioned earlier, to avoid over-fitting the minimization process has to be stopped at some point (stopping the minimization after a number of iterations could be seen also as a regularization process). In the range of iterations (6000-10000) where reliable solutions exist, the changes in the model are small in the central 4 arcminute region. It is also important to note that the increased raise in mass in the grid part of the solution after 2000 iterations (see figure 11) is driven mostly by the cells in the outermost region (beyond the Einstein radius, as shown more clearly below in figure 13). It can also be seen (see the inset in the upper right corner) that as the iteration number grows, the grid starts to accumulate mass in the transition

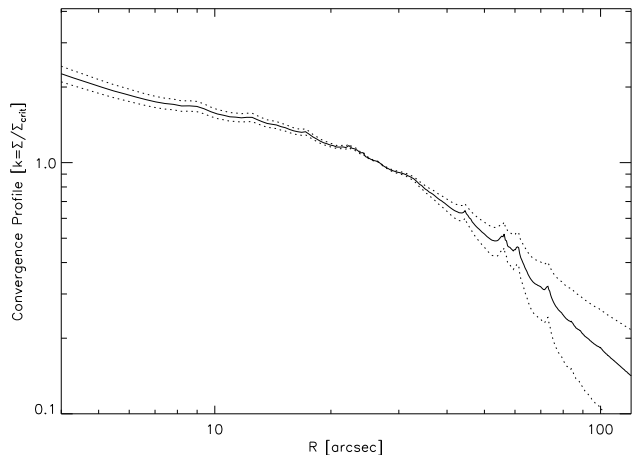


**Figure 15.** Average profile of the convergence from 40 independent solutions (solid line). The dotted lines represent the dispersion of these solutions.

phase between the  $6.66'$  region and the buffer zone. The bottom panel of figure 11 shows the quantity that is being minimized (properly re-scaled by some constant for clarity) as a function of the iteration number.

An alternative (and illustrative) way of looking at the evolution of the solution with the iteration number is shown in figure 13 where we show how the mass in individual cells evolve with the iteration number. We choose cells that are representative of a larger region. The top panel shows the typical behaviour of cells in the outer border of the buffer zone (they correspond to two diagonal cells at more than  $5'$  distance from the centre of the field of view). During the first few hundred iterations, the mass in these cells change very little but they become more *active* at later times when the solution at the central region has been constrained and remains more stable. As the iteration number grows, some cells in this region gain mass and some others lose it. Panel

b) shows what happens at the transition phase between the two resolutions. Again, this region plays a less important role at the beginning of the minimization but they become more *active* before the cells in the outer region. Also, it is interesting to see how both the large cell (dotted line) as well as the 4 neighbouring smaller cells (dashed lines) evolve simultaneously and also follow the same trend (increasing their mass). As can be seen from this figure and figure 12, the transition phase tends to accumulate mass as the iteration number grows. Panel c) shows what happens to the most central cells. The cell occupying the centre of the field of view corresponds to the solid line and the dotted lines correspond to the 4 cells which are closest to the central one. In this case the value on these cells converge much faster indicating that the algorithm naturally tends to put mass in the centre first and then moves outwards. This behaviour is not imposed but just happens naturally. The cells in the centre don't reach a stable point but neither does the  $C_1, C_2$  parameters shown in figure 11. Meanwhile, the profile seems to be less sensitive to the iteration number (see figure 12) indicating that there must be some trade-off mass between the grid and galaxies in order to compensate each other and keep the profile stable. Finally, panel d) shows an intermediate region between the centre of the field of view and the buffer zone. In this case, the evolution of the cells is more complex with no clear tendency. As in the case of the very central cells, the ones in this region evolve faster than the more distant ones (although not as fast as the most central cells). However, there seems to be more spatial variability in this region than in the centre and also less tendency to converge, especially those cells located beyond the Einstein radius (dashed lines) which at later times become more *active* under the influence of the WL data.

## 7.2 Dependency with the initial guess

When minimizing a multi-dimensional quadratic function one can find infinite solutions (for a given error) by varying the starting point of the minimization, all of them equally good in the sense of fitting the data set. The regions in the lens plane that are more sensitive to the data will converge quickly towards stationary points while regions with weaker sensitivity to the data might vary more from minimization to minimization or even not vary significantly and retain values close to their initial values (memory effect).

In figure 15 we show the average (solid) and 1-sigma region (dotted) of 40 reconstructions where in each one we change the initial condition by setting it to a vector of random numbers obtained from a Gaussian distribution. The dispersion of this Gaussian distribution is a random variable itself and is such that the total mass in the initial condition takes values in the range  $[\sim 0.2, \sim 2] \times 10^{15} M_{\odot}/h$ . Table 1 includes the values of the mean and errors as a function of distance. The solution retains some memory of the initial condition specially in the outer region where the constraints in the solution are the weakest. The most remarkable aspect of this plot is that all solutions seem to converge to the same profile in the range  $20'' - 30''$  defining a *stability* region for the solution.

This convergence is made more evident when looking at the 2D version of the above result. In figure 14 we show the average of the mass solutions (left panel) from which

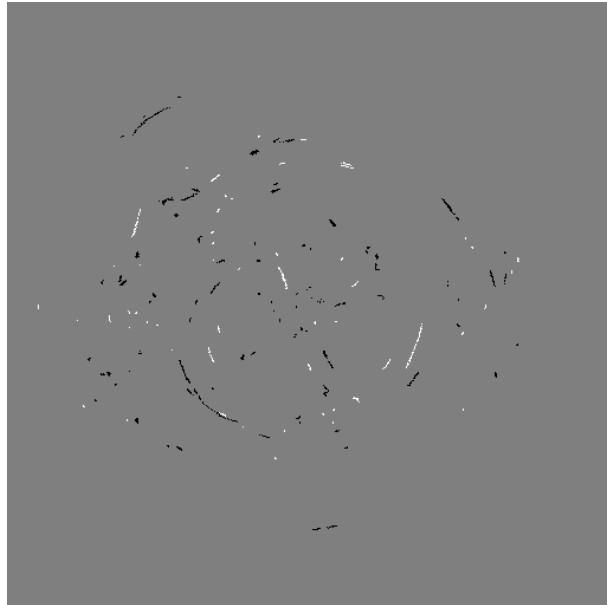


**Figure 16.** In black the original robust data set of 26 sources. In white we show the additional arcs that together with the previous 26 sources data set conform the extended 48 source data set of table 2 (sources 25 and 32 are not used). The field of view is  $3.33'$ .

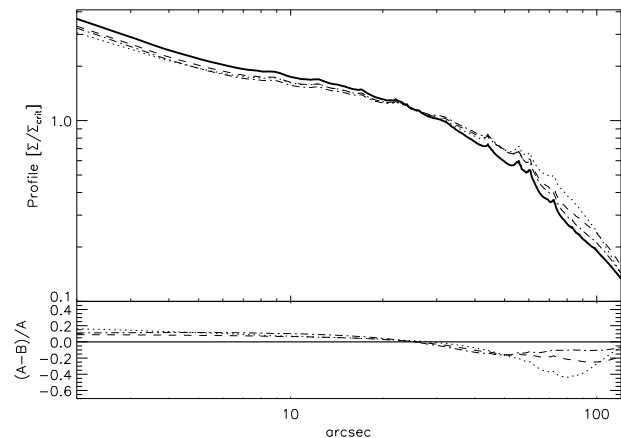


**Figure 17.** Comparison of the profiles obtained with different subsets of sources. The thick solid line corresponds to our reference solution obtained with the robust subset of 26 sources. The dotted line corresponds to the solution obtained with the full sample of 48 sources in table 2 (we exclude sources 25 and 32), or case i) (see text). The dashed line corresponds to the subset of 18 sources with spectroscopic redshifts or case ii) (see text) and the dot dashed line corresponds to the same initial set of 26 sources but the sources with photo-z taking substantially different redshifts, or case iii) (see text).

the above profile is derived. The middle panel shows the dispersion of the mass map and the right panel shows the signal-to-noise ratio (or SNR) defined as the ratio of the left and middle panels. There is a remarkably well defined circular region of high SNR around  $20'' - 30''$  from the centre. In this region, the solutions seem to be insensitive to the initial condition and they all render almost identical re-

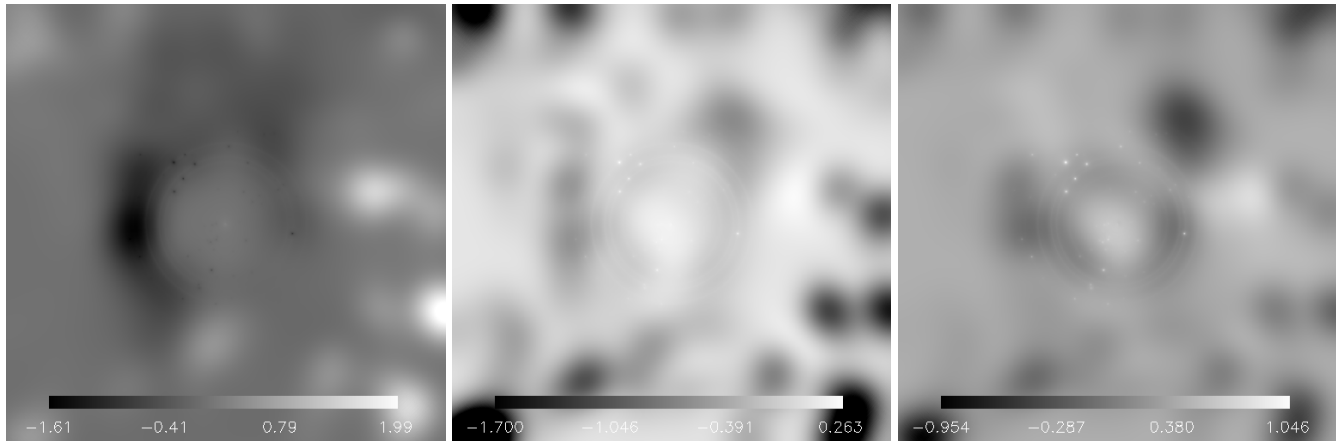


**Figure 18.** The figures show the difference between our reference solution and solutions obtained with three alternative subsets of sources. In all cases, the difference has been divided by the profile of the reference solution in order to visually maximize the differences. Hence a value of 2 in this graph means that in the difference of the two solutions (reference-alternative) there is 2 times the average mass of the profile for that radial bin etc. Some values (near the edges) have been saturated also for contrast purposes (the middle panel had a large negative deviation of -5 in the bottom left corner that was saturated to -1.7). The field of view corresponds to  $6.66'$  across. Left panel: case for which all 48 sources in table 2 are used (we exclude 25 and 32). Middle panel: case for which only the spectroscopic sub-sample of 18 sources is being used. Right panel: case for which the original 26 sub sample of sources is used but the sources with photometric redshift have different redshifts

sults. This region corresponds to a stability region of the solution where the profile is constrained very well. A second interesting aspect can be seen also in the SNR map. The high SNR of the dark matter blob, just south of the stability region, indicates that this might be a real substructure. This feature is not previously claimed and indeed parametric methods would not incorporate such dark sub-structure in principle and hence this is the first time it is revealed. Other interesting features emerge from the SNR map as potential real substructures of the cluster although with a lower SNR. The dispersion map shows how there is a region (upper-right quadrant) where the solutions fluctuate the most indicating that the mass map is less reliable in this region.

Finally, as expected (and already shown in the profile plot), the dispersion of the solutions in the central region (that is the cD galaxy) is larger, indicating therefore that our solution is not very sensitive to the very central region. This is due mostly to the fact that the larger arcs have a bigger weight in our solution. In a future paper we aim to study in more detail the most central region taking advantage of the stability region identified in this paper, and the possible implications for the mass profile of the cD galaxy.

### 7.3 Dependency with the number of systems and redshift

Identifying pairs of images in the strong lensing regime is not always free of subjectivity, resting on experience. A1689 is probably the most scrutinised lens, with hundreds arclets seen in the image, each with its own distortion that makes it difficult to find morphologically similar galaxies. The colors may also vary across the object due to differential magnification, and also because of overlap with other unrelated images or due to diffuse light in the cluster affecting the colours of relatively faint background galaxies. Spectroscopic redshifts of the arclets are often the best way to discriminate among different possibilities but even this does not always

settle the differences and furthermore neighbouring galaxies may become confused in the process if they have the same redshift to within the resolution limits. A good example of this is the difficulty to distinguish between systems 10 and 12 (both having basically the same spectroscopic redshift). Different authors have assigned the arclets to different systems (see table 2). In this section we explore the impact on the solution when we consider different subsets of arclets in our SL part of the data set.

In table 2 we compile all the systems that were found in the literature and we add several new systems (candidates) which are identified with our model. For the new systems we simply assume that they are at redshift  $z = 2$  when assessing their deflection angles. This is a useful approximation given the weak dependency of the deflection angles over the range  $z = [1, 3]$  (as shown by figure 9) and should be sufficient for our purposes. For our test we compare our reference solution described in section 5, which depended on only the 26 established systems, with new model solutions obtained for sets of images composed in the following 3 ways:

- (i) We consider an extended sample of systems listed in table 2 but exclude sources 25 and 32 for which multiple options exist for the same system. That is, we consider 48 sources out of the total 50 systems listed in table 2.
- (ii) As a second sub-sample we consider the subset of 18 sources from the original 26 sources of our reference solution for which spectroscopic redshifts are available, in table 2.
- (iii) The third sub-sample is the same as the original sample of 26 but for the sources with photometric redshifts we allow the redshifts to vary by a generous  $2\sigma$  error, adopting the  $\sigma$  values in Coe et al. (2010).

The extended data set of 48 systems is displayed in figure 16 where the original 26 systems are shown in black and the additional 22 systems in white. For each case, we reproduce the minimization process of section 5 that is, we adopt the same initial condition, number of iterations and make

**Table 1.** Mean profile and dispersion of the 40 solutions shown in figure 15. Both the mean profile and dispersion are given in units of  $\Sigma/\Sigma_{crit}$  with  $\Sigma_{crit}$  computed at  $z = 1.07$ . The last column shows the integrated (cylindrical) mass in units of  $10^{14}M_{\odot}/h$ .

arcsec	Mean	Disp.	M( $< r$ )
2.343	3.117	0.282	0.015
4.296	2.174	0.149	0.036
7.031	1.744	0.089	0.072
10.15	1.562	0.064	0.128
12.50	1.514	0.058	0.179
14.45	1.411	0.046	0.228
16.40	1.327	0.036	0.281
18.35	1.242	0.026	0.339
20.70	1.153	0.016	0.412
23.04	1.133	0.015	0.492
25.78	1.020	0.003	0.592
28.12	0.9477	0.006	0.680
30.46	0.9079	0.010	0.772
32.81	0.8616	0.015	0.869
35.15	0.7836	0.024	0.968
37.89	0.7198	0.032	1.083
40.62	0.6644	0.039	1.201
43.35	0.6308	0.044	1.320
46.09	0.5962	0.049	1.444
48.82	0.5367	0.057	1.565
51.56	0.4985	0.062	1.683
54.68	0.4976	0.063	1.819
57.81	0.4616	0.067	1.961
60.93	0.4619	0.067	2.097
64.06	0.3747	0.077	2.226
67.18	0.3324	0.081	2.341
70.70	0.3148	0.082	2.466
74.21	0.2976	0.081	2.589
77.73	0.2592	0.083	2.702
81.25	0.2402	0.083	2.808
84.76	0.2292	0.082	2.910
88.28	0.2145	0.080	3.011
92.18	0.2007	0.079	3.119
96.09	0.1900	0.078	3.225
100.0	0.1837	0.077	3.350
103.9	0.1725	0.076	3.432
107.8	0.1638	0.076	3.530
112.1	0.1554	0.075	3.634
116.4	0.1474	0.074	3.735
120.7	0.1409	0.074	3.829
125.3	0.1341	0.073	3.929
130.0	0.1285	0.072	4.040
135.1	0.1238	0.071	4.125
140.6	0.1204	0.070	4.234

use of both SL and WL data, in order to better examine model differences resulting from changes to the input the data set. Figure 17 shows this comparison in terms of the resulting mass profiles for the above cases.

Although there are some differences between the different solutions, the agreement is still remarkably good indicating that all data sets have enough common systems to produce similar results and/or that the solution is not very sensitive to modest changes in the redshift of some systems. This agreement indicates most simply that the systems in the extended sample naturally give good fits when the ref-

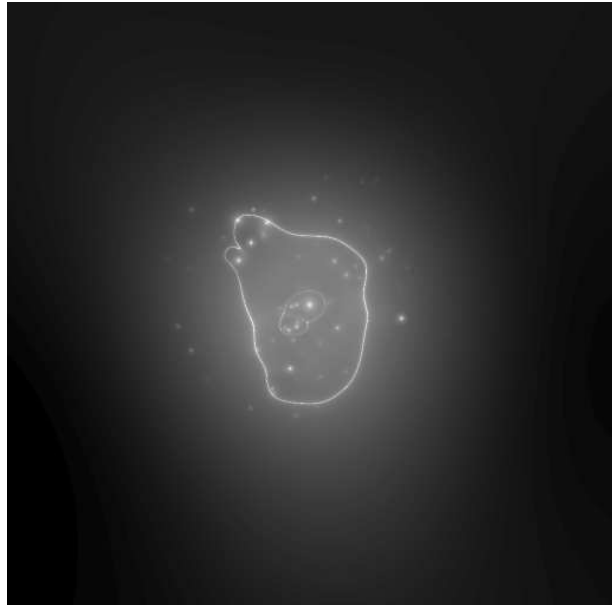


**Figure 19.** Mass and critical curve for a low resolution grid reconstruction (SL+WL). The cell sizes are 2.7 times larger in this case than in the reference solution.

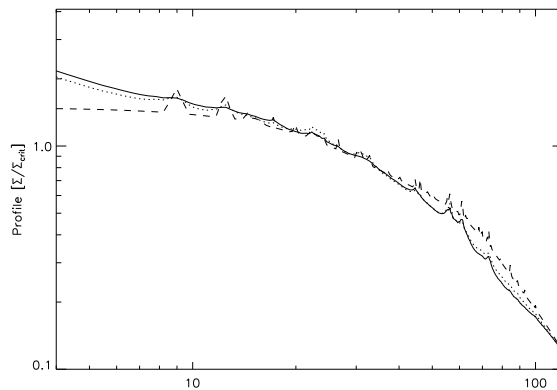


**Figure 20.** Change in reconstructed profile under three assumptions for the galaxies in the cluster. The solid line corresponds to the reference solution discussed above, the dotted line is for a different model where both the scale radius and total mass of the assumed NFW profile for the individual galaxies is changed by a factor  $\sim 2$ . The dashed line corresponds to another different realization of the masses in the galaxies (different also by a factor  $\sim 2$  with respect to the reference model) but their profiles are taken to the extreme case of delta functions. For the dashed line, there is a peak at the centre not shown in this plot that corresponds to the central galaxy.

erence solution is used. The last point is highlighted better in the last column of table 2 where we show the  $\Delta\beta$  for each arclet (and based on the reference solution). The  $\Delta\beta$  for a specific arclet  $i$  is defined as,

$$\Delta\beta_i(\text{arcsec}) = |\beta_i - \langle \beta \rangle| \quad (4)$$

where  $\beta_i$  is the predicted position of the arclet in the source plane when the reference solution is used and  $\langle \beta \rangle$  is the average of all the  $\beta_i$  for that system. As shown by the

values of  $\Delta\beta$  (expressed in arcseconds), most arclets lie at reasonable distances (few arcseconds) from their common centre in the source plane. Also, some systems appear to be problematic since they have large  $\Delta\beta$  values ( $10''$  or more, like in systems 25, 41, 44). These systems are either incorrect or our reference solution has substantial errors around the position of these systems. In other cases, like system 7, the arclet 7.3 ( $\Delta\beta = 9.3''$ ) is very close to the central cD galaxy and surrounded by multiple small sources (7.3, together with 8.5, and 19.5 where also rejected by (Coe et al. 2010)). It is possible that either the reference solution is not accurate at the centre (see discussion in section 7.2) or that 7.3 does not correspond with the source listed in table 2 but another one in the vicinity. If that's the case, this explains why 7.1 and 7.2 (which are clearly the same source), have also relatively high values of  $\Delta\beta$  since a bad association for 7.3 would bias  $\langle \beta \rangle$  and enhance the  $\Delta\beta$  for all the system.

Another interesting point from figure 17, is that the same stability region discussed in section 7.2 seems to be present when we change the SL data set, in the range  $20'' - 30''$ , where the solutions seem to be insensitive to the particular choice of data sets (among the 4 used in this comparison). This reinforces the idea that the solution is very well constrained in this regime ( $20'' - 30''$ ) and nearly insensitive to the intrinsic variation of the solutions.

Going beyond the differences in profile, we look at the mass maps for the above cases, comparing the reference solution and the 3 solutions described above. The result is shown in figure 18. In this case, the mass difference has been divided by the profile of the reference solution to increase contrast. Also, the middle panel has been saturated below values of -1.7 (the most negative value was -5) also for contrast purposes. The difference maps show where the surface mass density modifies itself in order to accommodate the possible changes in the data set and by extension, it marks the regions where extra caution needs to be taken into account when interpreting our main results, should the assumed original data set of 26 sources be compromised by systematics.

#### 7.4 Dependency on the grid configuration

The choice of grid resolution is an important decision that affects the performance of the reconstruction and must be made with some care. Ideally we would set a large number of cells that allows for a more detailed reconstruction. In practice however, a very large number of cells results only in a more noisy reconstruction that needs to be smoothed (regularized). The smoothed image captures the main eigenmodes of the solution that would be reconstructed also with a smaller number of cells. Also, a large number of cells implies a larger system of equations to resolve and a slower convergence. This limits the ability to explore the space of possible solutions which is important. On the other hand, a very small number of cells results in a more compact system of linear equations that can be resolved fast but at the expense of not capturing some of the potentially smaller scale details of the mass distribution and consequently forcing the entire mass distribution to adopt, often erroneous, distributions in order to fit the observations. As shown by Ponente & Diego (2011); Sendra et al. (2014), a low resolution grid can still produce reliable solutions but only after

allowing for a larger error in the reconstruction. Figure 19 shows the reconstructed solution when a lower resolution grid is used. In this case, the cell sizes are 2.7 times larger than the cell sizes in the reference solution. The solution resembles a smoothed version of the reference solution except in the radial critical curve where the lack of resolution does not allow for a detailed reconstruction.

A compromise alternative would be to use a multi-resolution grid where regions with a complex mass distribution are sampled with smaller cells and regions with a more smooth mass distribution (or less sensitive to the data) are sampled with larger cells. This possibility was explored in previous papers and produces satisfactory results although it is not entirely free of problems. In particular, the boundary region between regions of differing resolution tends to produce biased results (when tested with simulated data). The size of the cell normally introduces a prior in the solution. The reconstruction tends to put more mass in the smallest cells. This problem can be mitigated by solving in an iterative way where the first iteration assumes a regular grid (no prior) and the consecutive iterations increase the resolution in regions where the previous iteration found more mass. We have tried a battery of configurations and found that some of them (in particular those with multi-resolution) produce significant artifacts in the solution that need to be avoided. Regular grids are always more stable and reliable so in our particular case and due to the large field of view involved ( $10 \times 10$  arcminutes<sup>2</sup>) we choose a grid with good resolution in the central field of view ( $6 \times 6$  arcminutes<sup>2</sup>) and a lower resolution grid in the outer region (buffer zone). As expected, the solution near the boundary between the two regions produce artifacts as discussed above. We have checked that variations in the grid sizes of  $\sim 30\%$  with respect to our configuration, finding the results are nearly identical to the those presented in this paper. The cell sizes in the central part of the field of view are larger than the halo sizes of the galaxies (except the central galaxy) facilitating the orthogonality of the grid+galaxy base.

#### 7.5 Dependency with the parameters in the fiducial model

In order to test the sensitivity of the solution with the assumptions made for the adopted profile for the member galaxy component we compare the reference solution (solid line in figure 20) with two different assumptions regarding galaxy profiles. In the first case (dotted line in figure 20), we vary both the total mass of each galaxy and the scale radius by a factor  $\sim 2$  (above and below the values in the reference solution). In the second case, (dotted line in figure 20), we take the extreme (and unrealistic) case where all the masses in the galaxies are considered to be in just the centre of each galaxy (that is, galaxies are considered delta functions) and we also change their masses by a factor  $\sim 2$  with respect to the reference solution case. Remarkably, there is a region of stability (around  $20'' - 40''$ ) where the profile seems to be unaffected by the particular choice of the fiducial deflection field, even in the case where we consider unphysical assumptions for the fiducial field (delta function case for the galaxy masses). The dotted line (different NFW profiles for each galaxy) is almost indistinguishable from the reference solution. The dashed line case (delta functions) shows a relative

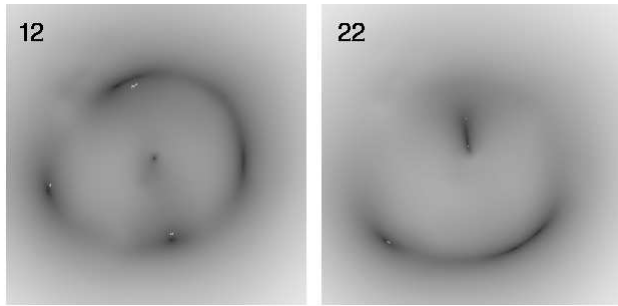


**Figure 21.** Predicted positions for systems 12 (left) and 22 (right). Data (arcs) are shown in white and model prediction in dark grey. For system 12, the solution correctly predicts an arclet (on the right side) identified by Limousin et al. (2007). For system 22, no counter-image is found at or near the position predicted by the solution (bottom right).

deficit in mass at very short radii, since all the mass of the central galaxy is concentrated at ( $r = 0$ ) which is not shown in the plot. At larger radii ( $r = 50'' - 100''$ ), the grid part of the solution shows an excess of mass (with respect to the reference solution). This might be due to a compensation effect of the unphysical nature of the delta function assumption although this is not observed at  $r = 20'' - 30''$ . When finding solutions we are of course dealing with the deflection field and since this relates to the gradient of the potential we may not be so surprised about the independence of the resulting model mass distribution with the choice of galaxy profile, since the galaxy potential is always extended even in the case of point masses. What is much more important here is that there is a contribution to the deflection field at the location of the member galaxies rather than the definition of the member galaxy mass profiles.

## 8 PREDICTED NEW SYSTEMS/ARCS

Using our solution (masses and source positions) for the case of SL+WL and 8000 iterations in section 5, we can predict the position of the multiple images for each source. In most cases, the agreement between these positions and the observed arcs is very good with typical errors of less than  $5''$  in the image plane but there are some deviations between the model and the data set that are interesting to explore in more detail. Disagreements between the predicted arcs and input data might reveal a systematic bias in the solution in that particular region of the image plane or even some tension between the identification of the multiple images in the data set. Also, new images (from a given system) might be identified with the new model. Figure 21 shows two of the most extreme cases where the disagreement between the prediction and the input data is more obvious. In dark grey we show the distance to the source position when that particular point in the image plane is projected back into the source plane at the redshift of the source. In white we show the observed position of the arcs in the original data set. We show the cases for systems 12 and 22. In system 12 we observe that the model predicts a new image on the right side of the field of view. Exploring this position in the original ACS image, the alleged new image is easily identified about  $10''$  north of the predicted position. Given the

fact that this is near a critical curve,  $10''$  are actually a relatively short distance along a critical curve. That new image was already correctly identified by Limousin et al. (2007). On the other hand, system 22 shows a clear prediction that is missing from our data set (and others in the literature). ACS data shows nothing that resembles this bright and distinctive source indicating that this is either a region that is near the regime where multiple sources merge and disappear (as suggested by the fact that by moving the source position a few arcseconds the predicted image disappears) or, maybe more likely, that the mass model is not very well constrained in this part of the lens plane.

In figure 22 we show additional examples of systems where the model accurately reproduces the positions (and also the extension) of the arcs in the data. Among these systems, we included also system 10, which has been redefined in this paper based on the new IR data. The new configuration of system 10 seems to be consistent with our model, with the exception of the arclet on the right side that is possibly affected by a nearby massive galaxy that our model fails to reproduce with enough accuracy.

From our reference model we have also identified a set of 11 new system candidates never published before. These new system candidates are listed in table 2 (in the appendix) with IDs ranging from 51 to 61. For all of these systems we have assumed a redshift of  $z = 2$  so the subset of new system candidates is naturally biased to have redshifts around this value. The stamps for the arclets in the new system candidates are shown in figures A1 and A2 (also in the appendix). The full collection of stamps for the arclets in table 2 can be found online at this website<sup>5</sup>.

## 9 CONCLUSIONS

We have presented a robust estimation of the dark matter distribution in the cluster A1689. We explore the range of variability of the solutions and identify a region of minimum variance where the solution is stable against changes in the configuration of the data set, the number of iterations, the grid resolution and, assumptions made of the fiducial deflection field. We also identify regions where the results should be taken with more caution. Our solution can be used to identify additional strongly lensed systems. We identify 11 new systems (candidates) and confirm some of the previous identifications like including the contentious system number 12 where our solution correctly predicts the fourth arclet identified in Limousin et al. (2007).

Even though the WL measurements have a typical sampling scale of  $1'$ , through the combination of the SL and WL data sets in the same minimization algorithm we manage to improve upon this resolution beyond the Einstein radius and be sensitive to smaller scales. This allows us to resolve details unseen before in the dark matter distribution around and beyond the Einstein radius, some of which have no obvious correlation with the luminous matter. At larger radii ( $r > 2$  arcmin) the sensitivity to smaller details weakens as the SL data set loses its capability to constrain the matter distribution at these distances.

<sup>5</sup> <http://max.ifca.unican.es/diego/FigsA1689/>



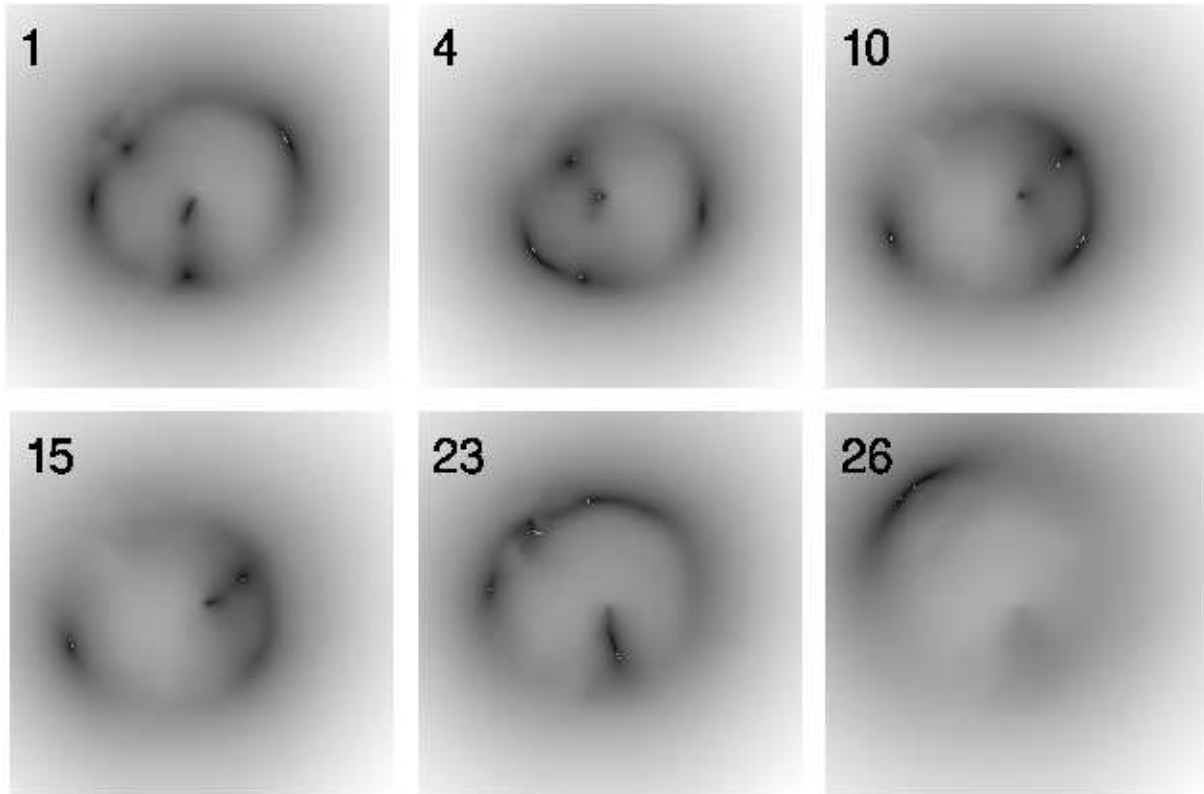


**Figure 22.** Some examples of systems where the model accurately predicts the arc positions. Most systems are reproduced with similar accuracy

A consequence of knowing the mass distribution of a lens is that it makes it possible to make predictions that can be used in other observations. For instance, we can derive redshifts for sources with unknown redshift by projecting the system back at different redshifts and finding the redshift at which the system *come into focus*. Figure 23 is an example for two of the photometric redshift systems in our sample. For these sources, the lens predicts lower redshifts than the photo-z although the predicted redshift is still consistent with the photo-z.

The mass model can be also used to impose constraints on the cosmological model, for instance through the  $f_k$  function as shown in section 6 although we also show that in order to get competitive constraints one should probably rely on stacking results from multiple clusters.

Finally, our free-form model allows us to determine the mass-to-light ratio of the main galaxies in the cluster. We find ratios that are generally consistent with earlier results found in the literature. However, with the exception of the central galaxy, the galaxies in our model assume the same  $M/L_B$  ratio limiting somehow the power of our study. A more detailed study where member galaxies are allowed to take on individual  $M/L_B$  ratios will be considered in a future work.

## 10 ACKNOWLEDGMENTS

J.M.D acknowledges support of the consolidator project CAD2010-00064 and AYA2012-39475-C02-01 funded by the

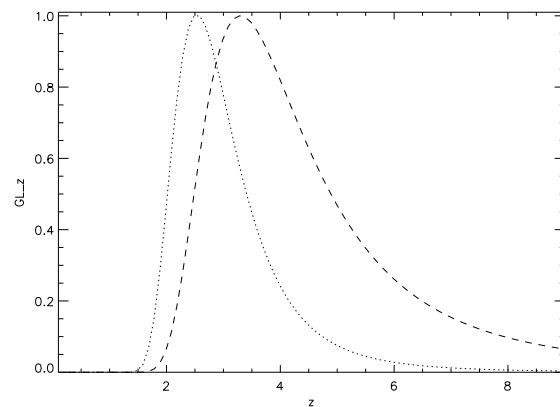


**Figure 23.** Gravitational lensing redshift prediction for systems 8 (dotted) and 9 (dashed) from our reference model.

Ministerio de Economía y Competitividad. JMD also acknowledges the hospitality of the Department of Physics and Astronomy at UPenn during part of this research. K.U. acknowledges partial support from the National Science Council of Taiwan (grant NSC100-2112-M-001-008-MY3). MS acknowledges financial support from the agreement ASI/INAF/023/12/0.

This paper has been typeset from a  $\text{\TeX}/\text{\LaTeX}$  file prepared by the author.

**REFERENCES**

- Alamo-Martínez K. A. et al., 2013, *ApJ*, 775, 20
- Bradley L. D. et al., 2008, *ApJ*, 678, 647
- Broadhurst, et al., 2005a, *ApJ*, 621, 53
- Broadhurst T., Takada M., Umetsu K., Kong X., Arimoto N., Chiba M., Futamase T., 2005b, *ApJ*, 619, L143
- Broadhurst T. J., Barkana R., 2008, *MNRAS*, 390, 1647
- Cain B., Schechter P. L., Bautz M. W., 2011, *ApJ*, 736, 43
- Clowe D., Bradač M., Gonzalez A. H., Markevitch M., Randall S. W., Jones C., Zaritsky D., 2006, *ApJ*, 648, L109
- Coe D., Benítez N., Broadhurst T., Moustakas L. A., 2010, *ApJ*, 723, 1678
- Coe D., Umetsu K., Zitrin A., Donahue M., Medezinski E., Postman M., 42 more authors., 2012, *ApJ*, 757, 22
- Coe D. et al., 2013, *ApJ*, 762, 32
- Diego J. M., Protopapas P., Sandvik H. B., Tegmark M., 2005a, *MNRAS*, 360, 477
- Diego J. M., Sandvik H. B., Protopapas P., Tegmark M., Benítez N., Broadhurst T., 2005b, *MNRAS*, 362, 1247
- Diego J. M., Tegmark M., Protopapas P., Sandvik H. B., 2007, *MNRAS*, 375, 958
- Frye B., Broadhurst T., Benítez N., 2002, *ApJ*, 568, 558
- Halkola A., Seitz S., Pannella M., 2006, *MNRAS*, 372, 1425
- Jullo E., Kneib J.-P., 2009, *MNRAS*, 395, 1319
- Jullo E., Natarajan P., Kneib J.-P., D'Aloisio A., Limousin M., Richard J., Schimd C., 2010, *Science*, 329, 924
- Kassiola A., Kovner I., Fort B., 1992, *ApJ*, 400, 41
- Kneib J.-P., Ellis R. S., Smail I., Couch W. J., Sharples R. M., 1996, *ApJ*, 471, 643
- Koekemoer A. M., et al., 2002, *HST Dither Handbook*
- Lemze D., Barkana R., Broadhurst T. J., Rephaeli Y., 2008, *MNRAS*, 386, 1092
- Lemze D., Broadhurst T., Rephaeli Y., Barkana R., Umetsu K., 2009, *ApJ*, 701, 1336
- Leonard A., Goldberg D. M., Haaga J. L., Massey R., 2007, *ApJ*, 666, 51
- Leonard A., King L. J., Goldberg D. M., 2011, *MNRAS*, 413, 789
- Limousin M. et al., 2007, *ApJ*, 668, 643
- Lubini M., Sereno M., Coles J., Jetzer P., Saha P., 2014, *MNRAS*, 437, 2461
- Natarajan P., Kneib J.-P., Smail I., Treu T., Ellis R., Moran S., Limousin M., Czoske O., 2009, *ApJ*, 693, 970
- Oguri M., Takada M., Umetsu K., Broadhurst T., 2005, *ApJ*, 632, 841
- Okabe N., Futamase T., Kajisawa M., Kuroshima R., 2013, *ArXiv e-prints*
- Peng E.-H., Andersson K., Bautz M. W., Garmire G. P., 2009, *ApJ*, 701, 1283
- Ponente P. P., Diego J. M., 2011, *A&A*, 535, A119
- Riemer-Sørensen S., Paraficz D., Ferreira D. D. M., Pedersen K., Limousin M., Dahle H., 2009, *ApJ*, 693, 1570
- Sendra I., Diego J. M., Broadhurst T., Lazkoz R., 2014, *MNRAS*, 437, 2642
- Sereno M., Ettori S., Umetsu K., Baldi A., 2013, *MNRAS*, 428, 2241
- Sereno M., Umetsu K., 2011, *MNRAS*, 416, 3187
- Umetsu K., Broadhurst T., 2008, *ApJ*, 684, 177
- Umetsu K., Broadhurst T., Zitrin A., Medezinski E., Hsu L.-Y., 2011, *ApJ*, 729, 127
- Zekser K. C. et al., 2006, *ApJ*, 640, 639
- Zheng W. et al., 2012, *Nature*, 489, 406
- Zitrin A., Broadhurst T., Barkana R., Rephaeli Y., Benítez N., 2011, *MNRAS*, 410, 1939
- Zitrin A., Broadhurst T., Rephaeli Y., Sadeh S., 2009, *ApJ*, 707, L102
- Zitrin A. et al., 2010, *MNRAS*, 408, 1916

**APPENDIX A: COMPILATION OF ARC POSITIONS AND STAMPS**

**Table A1.** Full strong lensing data set. The second column shows the new system ID following the original notation of (Broadhurst & et al. 2005a). The third column shows the original notation (Broadhurst & et al. 2005a). Systems not present in the original paper are left blank in this column. The fourth column indicates previous papers in the literature where that system was identified, B05 is for (Broadhurst & et al. 2005a), L07 for (Limousin et al. 2007), C10 for (Coe et al. 2010) and D14 for the present paper. Fifth and sixths columns show the coordinates of each arclet. Discrepancies with some of the positions published in (Coe et al. 2010) have been resolved by (D. Coe, private communication) and are corrected in the present version of the table. The seventh column includes the redshifts used in our study. A negative sign indicates that they are photometric redshifts. The last column shows the  $\Delta\beta$  derived from our reference model, see equation 4

i	ID	B05	REF	RAJ2000(h:m:s)	DECJ2000(d:m:s)	z	$\Delta\beta$
1	1.1	1.1	B05	13:11:26.257	-1:19:58.753	3.04	1.03
2	1.2	1.2	B05	13:11:26.088	-1:20:02.261	3.04	0.73
3	1.3	1.3	B05	13:11:29.584	-1:21:09.475	3.04	2.50
4	1.4	1.4	B05	13:11:32.870	-1:20:29.403	3.04	1.27
5	1.5	1.5	B05	13:11:31.742	-1:20:07.998	3.04	3.98
6	1.6	1.6	B05	13:11:29.661	-1:20:40.413	3.04	2.44
7	2.1	2.1	B05	13:11:26.331	-1:19:57.450	2.53	0.92
8	2.2	2.2	B05	13:11:32.771	-1:20:27.494	2.53	1.78
9	2.3	2.3	B05	13:11:31.780	-1:20:09.147	2.53	3.42
10	2.4	2.4	B05	13:11:29.619	-1:21:08.008	2.53	2.32
11	2.5	2.5	B05	13:11:29.686	-1:20:41.365	2.53	2.02
12	3.1	3.1	B05	13:11:31.850	-1:20:29.520	-5.47	2.30
13	3.2	3.2	B05	13:11:31.979	-1:20:35.287	-5.47	1.29
14	3.3	3.3	B05	13:11:31.492	-1:20:58.040	-5.47	3.33
15	4.1	4.1	B05	13:11:31.978	-1:20:59.355	1.10	0.18
16	4.2	4.2	B05	13:11:30.326	-1:21:14.026	1.10	2.24
17	4.3	4.3	B05	13:11:30.565	-1:20:10.322	1.10	3.02
18	4.4	4.4	B05	13:11:26.094	-1:20:37.422	1.10	0.94
19	4.5	4.5	B05	13:11:29.653	-1:20:31.357	1.10	2.23
20	5.1	5.1	B05	13:11:28.873	-1:20:50.776	2.60	2.10
21	5.2	5.2	B05	13:11:29.032	-1:20:46.153	2.60	3.10
22	5.3	5.3	B05	13:11:33.927	-1:20:22.919	2.60	5.20
23	6.1	6.1	B05	13:11:30.555	-1:19:39.995	1.10	1.57
24	6.2	6.2	B05	13:11:33.154	-1:20:14.174	1.10	2.70
25	6.3	6.3	B05	13:11:32.558	-1:19:56.506	1.10	1.45
26	6.4	6.4	B05	13:11:32.289	-1:20:00.857	1.10	2.72
27	7.1	7.1	B05	13:11:25.256	-1:20:53.843	4.87	7.68
28	7.2	7.2	B05	13:11:30.478	-1:20:15.902	4.87	3.18
29	7.3	7.3	B05	13:11:29.627	-1:20:26.870	4.87	9.33
30	8.1	8.1	B05	13:11:32.105	-1:20:52.909	-2.67	1.32
31	8.2	8.2	B05	13:11:31.210	-1:21:07.541	-2.67	3.41
32	8.3	8.3	B05	13:11:31.313	-1:20:16.078	-2.67	2.57
33	8.4	8.4	B05	13:11:25.337	-1:20:22.162	-2.67	2.87
34	8.5	8.5	B05	13:11:30.136	-1:20:32.494	-2.67	6.61
35	9.1	9.1	B05	13:11:30.115	-1:19:50.652	-5.16	7.14
36	9.2	9.2	B05	13:11:33.328	-1:20:52.335	-5.16	1.31
37	9.3	9.3	B05	13:11:28.554	-1:21:17.805	-5.16	2.08
38	9.4	9.4	B05	13:11:26.079	-1:20:28.927	-5.16	4.37
39	10.1	10.1	B05	13:11:33.786	-1:20:52.855	1.83	1.78
40	10.2	10.2	B05	13:11:27.857	-1:20:14.477	1.83	3.89
41	10.3	10.3	B05	13:11:29.125	-1:20:29.744	1.83	2.67
42 <sup>a</sup>	10.4	12.2	B05	13:11:27.166	-1:20:56.946	1.83	3.72
43 <sup>b</sup>	10.5	12.3	B05	13:11:27.033	-1:20:53.910	1.83	4.57
44	11.1	11.1	B05	13:11:33.149	-1:21:08.754	2.50	2.35
45	11.2	11.2	B05	13:11:28.866	-1:20:03.292	2.50	1.54
46	11.3	11.3	B05	13:11:29.300	-1:20:28.381	2.50	2.05
47	12.1	12.1	B05	13:11:30.171	-1:19:53.471	1.82	6.34
48	12.2	12.4	B05	13:11:28.771	-1:21:12.265	1.82	2.66
49 <sup>c</sup>	12.3	31.2	C10	13:11:33.081	-1:20:46.390	1.82	1.31

<sup>a</sup> System has been re-organized

<sup>b</sup> System has been re-organized

<sup>c</sup> System has been re-organized. New arclet candidate

**Table A1.** cont.

i	ID	B05	REF	RAJ2000(h:m:s)	DECJ2000(d:m:s)	z	$\Delta\beta$
50 <sup>a</sup>	12.4	31.4	C10	13:11:26.303	-1:20:24.080	1.82	2.64
51	13.1	13.1	B05	13:11:32.631	-1:19:26.371	-1.02	1.05
52	13.2	13.2	B05	13:11:32.795	-1:19:27.831	-1.02	0.97
53	13.3	13.3	B05	13:11:33.200	-1:19:33.134	-1.02	2.03
54	14.1	14.1	B05	13:11:28.835	-1:21:43.802	3.40	0.65
55	14.2	14.2	B05	13:11:29.266	-1:21:44.623	3.40	0.65
56	15.1	15.1	B05	13:11:27.882	-1:20:17.196	1.80	0.50
57	15.2	15.2	B05	13:11:33.883	-1:20:53.311	1.80	1.03
58	15.3	15.3	B05	13:11:29.046	-1:20:29.573	1.80	0.96
59	16.1	16.1	B05	13:11:27.790	-1:20:27.319	-2.01	1.63
60	16.2	16.2	B05	13:11:28.721	-1:20:30.546	-2.01	3.14
61	16.3	16.3	B05	13:11:34.205	-1:20:48.402	-2.01	1.55
62	17.1	17.1	B05	13:11:30.463	-1:20:26.890	2.60	3.04
63	17.2	17.2	B05	13:11:30.196	-1:20:29.765	2.60	6.11
64	17.3	17.3	B05	13:11:24.787	-1:20:43.865	2.60	9.12
65	18.1	18.1	B05	13:11:28.052	-1:20:11.540	1.80	1.23
66	18.2	18.2	B05	13:11:33.627	-1:20:56.539	1.80	0.86
67	18.3	18.3	B05	13:11:29.169	-1:20:29.392	1.80	0.43
68	19.1	19.1	B05	13:11:31.440	-1:20:24.597	2.60	3.53
69	19.2	19.2	B05	13:11:25.047	-1:20:22.003	2.60	5.47
70	19.3	19.3	B05	13:11:31.762	-1:21:01.315	2.60	3.61
71	19.4	19.4	B05	13:11:31.859	-1:20:59.131	2.60	2.02
72	19.5	19.5	B05	13:11:30.017	-1:20:35.961	2.60	3.05
73	21.1	21.1	B05	13:11:30.833	-1:20:47.776	-1.78	1.45
74	21.2	21.2	B05	13:11:30.608	-1:20:46.743	-1.78	2.42
75	21.3	21.3	B05	13:11:25.061	-1:20:13.207	-1.78	3.51
76	22.1	22.1	B05	13:11:29.493	-1:20:10.794	1.70	3.73
77	22.2	22.2	B05	13:11:29.423	-1:20:25.762	1.70	1.71
78	22.3	22.3	B05	13:11:32.222	-1:21:17.917	1.70	4.69
79	23.1	23.1	B05	13:11:29.337	-1:20:12.016	-2.00	2.94
80	23.2	23.2	B05	13:11:29.361	-1:20:24.891	-2.00	1.06
81	23.3	23.3	B05	13:11:32.465	-1:21:17.199	-2.00	3.45
82	24.1	24.1	B05	13:11:28.998	-1:20:58.177	2.60	0.06
83	24.2	24.2	B05	13:11:31.871	-1:19:52.560	2.60	0.95
84	24.3	24.3	B05	13:11:30.101	-1:19:36.140	2.60	3.12
85	24.4	24.4	B05	13:11:33.525	-1:20:21.863	2.60	3.32
86	24.5	24.5	B05	13:11:29.436	-1:20:38.999	2.60	7.13
87 <sup>b</sup>	25.1	25.1	B05	13:11:28.302	-1:20:36.990	2.50	9.30
88 <sup>c</sup>	25.2	25.2	B05	13:11:34.455	-1:20:35.581	2.50	6.71
89 <sup>d</sup>	25.2	56.1	D14	13:11:33.970	-1:20:41.300	2.50	22.47
90 <sup>e</sup>	25.2	45.2	C10	13:11:35.489	-1:20:32.950	2.50	37.17
91	28.1	28.1	B05	13:11:28.105	-1:20:12.907	-5.45	0.83
92	28.2	28.2	B05	13:11:34.067	-1:21:02.009	-5.45	2.62
93 <sup>f</sup>	28.3	28.3	C10	13:11:29.100	-1:20:28.610	-5.45	2.11
94	29.1	29.1	B05	13:11:29.033	-1:20:59.909	2.50	1.04
95	29.2	29.2	B05	13:11:29.845	-1:19:36.215	2.50	3.95
96	29.3	29.3	B05	13:11:31.952	-1:19:54.565	2.50	1.44
97	29.4	29.4	B05	13:11:33.433	-1:20:22.815	2.50	3.72
98	29.5	29.5	B05	13:11:29.537	-1:20:38.603	2.50	9.75
99	30.1	30.1	B05	13:11:32.228	-1:19:21.826	3.00	1.95
100	30.2	30.2	B05	13:11:32.990	-1:19:28.069	3.00	0.49
101	30.3	30.3	B05	13:11:33.461	-1:19:34.691	3.00	2.44
102	32.1		C10	13:11:31.998	-1:20:05.530	3.00	3.69
103	32.2		C10	13:11:33.023	-1:20:22.900	3.00	1.10

<sup>a</sup> New arclet candidate not used in our primary analysis<sup>b</sup> Original arclet not used in our analysis<sup>c</sup> Original arclet not used in our analysis. Multiple possibilities for this arclet.<sup>d</sup> New arclet not used in our primary analysis. Multiple possibilities for this arclet.<sup>e</sup> New arclet not used in our primary analysis. Multiple possibilities for this arclet.<sup>f</sup> New arclet not used in our primary analysis

Table A1. cont.

i	ID	B05	REF	RAJ2000(h:m:s)	DECJ2000(d:m:s)	z	$\Delta\beta$
104	32.3		C10	13:11:29.396	-1:21:04.830	3.00	0.12
105	32.4		C10	13:11:29.611	-1:20:45.350	3.00	3.53
106 <sup>a</sup>	32.5		L07	13:11:26.407	-1:19:59.600	3.00	8.00
107 <sup>b</sup>	32.5		D14	13:11:27.470	-1:19:41.520	3.00	6.86
108	33.1		C10	13:11:28.256	-1:21:02.660	4.58	7.29
109	33.2		C10	13:11:34.460	-1:20:35.600	4.58	7.29
110	35.1		C10	13:11:28.367	-1:21:01.350	1.90	2.45
111	35.2		C10	13:11:33.765	-1:20:34.520	1.90	4.12
112	35.3		C10	13:11:29.238	-1:20:36.660	1.90	5.60
113	36.1		C10	13:11:31.373	-1:19:47.940	3.00	0.26
114	36.2		C10	13:11:31.493	-1:19:49.390	3.00	0.26
115	40.1		C10	13:11:30.067	-1:20:14.040	2.52	4.98
116	40.2		C10	13:11:25.983	-1:21:05.290	2.52	4.98
117	41.1		C10	13:11:27.679	-1:20:50.710	-2.50	12.23
118	41.2		C10	13:11:35.329	-1:20:31.380	-2.50	29.37
119	41.3		C10	13:11:28.769	-1:20:36.120	-2.50	17.19
120	42.1		C10	13:11:28.479	-1:19:44.980	-2.00	4.31
121	42.2		C10	13:11:31.077	-1:19:55.520	-2.00	5.44
122	42.3		C10	13:11:33.317	-1:20:37.890	-2.00	1.60
123	42.4		C10	13:11:28.842	-1:21:09.490	-2.00	1.22
124	44.1		C10	13:11:28.324	-1:20:23.380	-2.00	11.81
125	44.2		C10	13:11:34.338	-1:21:04.010	-2.00	11.81
126	46.1		C10	13:11:31.476	-1:20:49.190	-2.50	4.65
127	46.2		C10	13:11:24.766	-1:20:15.980	-2.50	4.65
128	48.1		C10	13:11:31.365	-1:20:38.470	-2.00	2.29
129	48.2		C10	13:11:24.911	-1:20:19.820	-2.00	2.29
130	49.1		C10	13:11:28.660	-1:20:15.470	-2.00	2.76
131	49.2		C10	13:11:33.376	-1:21:08.730	-2.00	2.76
132	50.1		C10	13:11:32.387	-1:20:45.600	-2.50	2.16
133	50.2		C10	13:11:30.828	-1:21:11.080	-2.50	2.13
134	50.3		C10	13:11:31.467	-1:20:15.660	-2.50	0.05
135	51.1		D14	13:11:33.650	-1:20:17.710	-2.00	3.05
136	51.2		D14	13:11:30.470	-1:19:34.740	-2.00	2.09
137	51.3		D14	13:11:32.050	-1:19:45.140	-2.00	1.51
138	52.1		D14	13:11:29.480	-1:19:35.920	-1.80	1.10
139	52.2		D14	13:11:33.090	-1:20:17.170	-1.80	1.10
140	53.1		D14	13:11:31.500	-1:20:06.590	-3.00	1.72
141	53.2		D14	13:11:32.920	-1:20:36.490	-3.00	5.26
142	53.3		D14	13:11:30.120	-1:21:21.210	-3.00	12.79
143	53.4		D14	13:11:25.910	-1:20:08.430	-3.00	6.02
144	54.1		D14	13:11:31.480	-1:20:09.980	-2.00	1.75
145	54.2		D14	13:11:32.690	-1:20:37.270	-2.00	1.34
146	54.3		D14	13:11:29.900	-1:21:12.120	-2.00	2.66
147	54.4		D14	13:11:25.770	-1:20:11.550	-2.00	4.04
148	55.1		D14	13:11:30.920	-1:20:18.690	-1.50	2.04
149	55.2		D14	13:11:25.480	-1:20:31.180	-1.50	2.04
150	56.1		D14	13:11:28.558	-1:19:43.790	-2.00	5.36
151	56.2		D14	13:11:31.366	-1:19:59.450	-2.00	5.03
152	56.3		D14	13:11:33.165	-1:20:33.110	-2.00	1.69
153	56.4		D14	13:11:29.049	-1:21:06.660	-2.00	2.17
154	57.1		D14	13:11:31.206	-1:19:54.500	-2.00	3.72
155	57.2		D14	13:11:33.326	-1:20:33.100	-2.00	2.55
156	57.3		D14	13:11:28.823	-1:21:05.100	-2.00	2.52
157	57.4		D14	13:11:29.953	-1:19:43.780	-2.00	1.72
158	58.1		D14	13:11:33.165	-1:20:03.730	-2.00	6.87
159	58.2		D14	13:11:29.351	-1:20:51.190	-2.00	6.87
160	59.1		D14	13:11:26.920	-1:20:39.240	-2.00	1.19
161	59.2		D14	13:11:27.136	-1:20:48.140	-2.00	1.19
162	60.1		D14	13:11:29.988	-1:20:19.280	-2.00	0.51
163	60.2		D14	13:11:29.893	-1:20:23.050	-2.00	0.51
164	61.1		D14	13:11:32.277	-1:21:22.900	-2.00	7.83
165	61.2		D14	13:11:29.524	-1:20:10.240	-2.00	7.83

<sup>a</sup> Multiple possibilities for this arclet

<sup>b</sup> Multiple possibilities for this arclet

